Q. J. R. Meteorol. Soc. (1999), **125**, pp. 837–869

A simple radiative–convective model with a hydrological cycle and interactive clouds

By MICHAEL A. KELLY*, DAVID A. RANDALL and GRAEME L. STEPHENS
Colorado State University, USA

(Received 5 June 1997; revised 3 April 1998)

SUMMARY

We have developed a simple, analytically tractable radiative–convective model of the tropical climate system that includes an explicit moisture budget, a simple convection parametrization, a simple but physically based radiation parametrization, and interactive clouds. The underlying surface is assumed to be ocean. The model includes prognostic equations for the sea surface temperature and the vertically integrated water vapour content. A stratosphere in radiative equilibrium limits the depth of the convective layer. The lower-tropospheric lapse rate, surface evaporation rate, and clear-sky long-wave and short-wave radiative fluxes at the surface and the top of the atmosphere are determined as functions of the sea surface temperature and precipitable water only. The radiative–convective equilibria of the model atmosphere resemble the observed tropical climate, if realistic sea surface temperatures are prescribed. However, cloud-free radiative–convective equilibria of the tropical atmosphere–ocean system do not occur for realistic values of the surface albedo. When cloud radiative effects are included, the model produces radiative–convective equilibria that are unrealistically warm. With prescribed realistic lateral energy and moisture transports, however, the equilibria of the model are realistic.

KEYWORDS: Equilibrium Tropical atmosphere

1. INTRODUCTION

A variety of different model types have been used to study climate, including general circulation models (GCMs; e.g. Randall *et al.* 1989), radiative–convective models (Manabe and Wetherald 1967; Ramanathan and Coakley 1978), and energy-balance models (e.g. North 1975). Atmospheric and coupled ocean–atmosphere GCMs provide the most comprehensive and detailed climate simulations, but GCMs are expensive to run and their results are often difficult to interpret. Untangling the connections among the various physical processes in GCMs can be almost as difficult as untangling those in nature.

Energy-balance models and radiative–convective models offer simplicity and low computational cost but with much less quantitative accuracy. These simple models provide some qualitative insights which can be compared to observations and to GCM simulations. On the other hand, their simplicity severely limits their realism. In particular, energy-balance models do not represent the atmosphere's vertical structure, which means that quantities such as meridional energy transport must be parametrized in terms of the surface temperature only; most energy-balance models also lack a hydrologic cycle.

Radiative–convective models use multiple layers (often several tens of them) to explicitly represent the vertical structure of the atmosphere. Although early versions contained no hydrological cycle, modern radiative–convective models have corrected this deficiency (e.g. Renno *et al.* 1994; Emanuel 1991). Many radiative–convective models still exclude cloud radiative effects, which strongly influence climate. Current radiative–convective models also tend to be too complicated to study analytically.

The fundamental role of the hydrological cycle in determining the tropical climate is now widely recognized (e.g. Webster 1994). The connections between clouds and the tropical energy budget are particularly important—connections that involve a number of complex processes. It is of paramount importance to understand the processes that establish how the large-scale environment controls convection, and the extent to which the convection modulates radiative transfer (e.g. Lau *et al.* 1994; Wong *et al.* 1993).

* Corresponding author: Department of Atmospheric Science, Colorado State University, Fort Collins, Colorado 80523, USA.

Our goal in this study has been to develop the simplest possible radiative–convective model that can represent the tropical atmosphere of earth. We use the model to develop ideas about the interactions of various physical processes, which can then be tested against observations and the results of simulations with more realistic models. We introduce a simplified cloud radiative transfer scheme, ignoring the radiative effects of liquid-water clouds and parametrizing the formation of ice clouds in terms of the precipitation rate. The latter is determined by assuming that convection keeps the vertical profile close to moist neutrality. The model could be altered to include more horizontal degrees of freedom, e.g. by considering separate ascending and descending regions, as in the studies of Betts and Ridgeway (1989) and Pierrehumbert (1995). This is a worthy objective for the future, but we choose to postpone such complexities until we have fully investigated the radiative–convective equilibria of the current version.

Through the application of this model, we have been able to identify and investigate a number of issues concerning the links between convection and radiation in the tropical atmosphere. We show that the isolated tropical ocean–atmosphere system cannot reach equilibrium in the absence of cloud radiative effects. The column water vapour reaches extremely large values, and a "runaway greenhouse" results (Ingersoll 1969). We also show that the addition of cloud radiative effects allows the model to reach equilibrium for low wind speeds and with relatively efficient removal of the ice-water path by stratiform precipitation. The model's equilibrium solutions are quite sensitive to the short-wave and long-wave cloud optical depths, which are parametrized as functions of the ice-water path. A current practice is to assume that the ratio of these optical depths is near two but, as discussed later, measurements of this ratio vary considerably.

The effects of radiatively active clouds on the depth and thermal structure of the tropical troposphere are still not well understood. Recently, Thuburn and Craig (1997) compared results from a GCM and a radiative–convective model to show that the tropopause height is sensitive to the specified surface temperature and to the specified water vapour distribution. Only clear-sky results were reported, however, so the influence of cloud radiative effects on tropopause height remain unknown. The present study seeks to explore aspects of these issues in a rudimentary way using a simple model of convection and cloud radiative processes. We show how cloud radiative effects influence the tropopause height and tropopause temperature.

This paper presents the formulation and results from a new radiative–convective model which contains an explicit hydrological cycle and radiatively active clouds, yet remains simple enough for its behaviour to be studied analytically. The model also includes an explicit cumulus parametrization that allows for a variable lapse rate and variable absolute and relative humidities. The tropopause height and temperature are predicted on the basis of the requirement of temperature continuity at the base of a two-layer stratosphere in radiative equilibrium.

The organization of this paper is as follows. Section 2 outlines the basic structure of our model. The parametrized hydrological cycle is explained in section 3; section 4 describes the radiation parametrization; and section 5 discusses the calculation of tropopause height and temperature. Section 6 discusses radiative–convective equilibria of the model, while section 7 describes how the results change for prescribed lateral energy and moisture transports. Section 8 presents a summary and conclusions.

2. Basic structure

Consider a layer of air that is convectively coupled to the tropical ocean, extending from the surface, $z = 0$, to a height $z = z_C$, below which the convection is confined. We

describe this physical system using two prognostic variables, representing the ocean surface temperature, T_S, and the precipitable water, W.

We enforce energy conservation for the convectively active layer of the atmosphere. The moist static energy is defined by

$$h \equiv s + Lq, \tag{1}$$

where the dry static energy is represented by $s \equiv c_p T + gz$, L is the latent heat of condensation, c_p is the heat capacity of air at constant pressure, T is the temperature, g is the acceleration of gravity, and q is the water vapour mixing ratio. Recall that h is approximately conserved under both moist adiabatic and dry adiabatic processes, and that s is approximately conserved under dry adiabatic processes. The tropospheric vertically integrated moist static energy, H, is defined by

$$H \equiv \int_0^{z_C} h\rho \, dz = \int_0^{z_C} s\rho \, dz + LW, \tag{2}$$

and is governed by

$$\frac{dH}{dt} - \rho_C h_C \frac{dz_C}{dt} = (-\mathcal{S}_S + \mathcal{R}_S + \mathcal{Q}_H + L\mathcal{E}) + (\mathcal{S}_C - \mathcal{R}_C), \tag{3}$$

where ρ is the air density, t is time, $\mathcal{S}_C$ is the net solar radiation absorbed at and below level z_C (including that absorbed by the ocean), and $\mathcal{R}_C$ is the net long-wave radiation passing upward through z_C. $\mathcal{S}_S$ is the solar radiation absorbed by the ocean; $\mathcal{R}_S$ is the net upward infrared radiation at the sea surface; $\mathcal{Q}_H$ is the surface sensible-heat flux; and $\mathcal{E}$ is the rate of evaporation of sea water. There are no latent-heating terms on the right-hand side (RHS) of (3), because moist static energy is conserved under moist adiabatic processes. The second term on the left-hand side (LHS) represents the effects of z_C moving with respect to the air. As discussed later, (3) is used diagnostically rather than prognostically.

We assume that the tropopause occurs at level z_C and that the stratosphere is in radiative equilibrium. As described in section 5, the constraints of stratospheric radiative equilibrium and temperature continuity are used to determine the tropopause temperature and height.

The prognostic equation for the surface temperature is

$$\rho_w C D \frac{dT_S}{dt} = \mathcal{S}_S - \mathcal{R}_S - \mathcal{Q}_H - L\mathcal{E}, \tag{4}$$

where ρ_w is the density of water, C is the heat capacity of ocean water per unit depth, and D is the depth of the ocean mixed layer (specified and assumed constant).

The moisture budget of the atmosphere is expressed by

$$\frac{d}{dt}(W + IWP) - \rho_C q_{T,C} \frac{dz_C}{dt} = \mathcal{E} - \mathcal{P}, \tag{5}$$

where IWP is the ice-water path, $\mathcal{P}$ is the precipitation rate, and $q_{T,C}$ is the total water mixing ratio. The second term on the LHS of (5) represents the effects of the movement of z_C with respect to the air. Here we do not include a liquid-water path, because we limit the cloud types under consideration to precipitating upper-tropospheric convective anvils which are composed of ice crystals only. We assume that the convective layer is sufficiently deep so that $q_{T,C}$ is very small; then (5) reduces to

$$\frac{d}{dt}(W + IWP) \cong \mathcal{E} - \mathcal{P}. \tag{6}$$

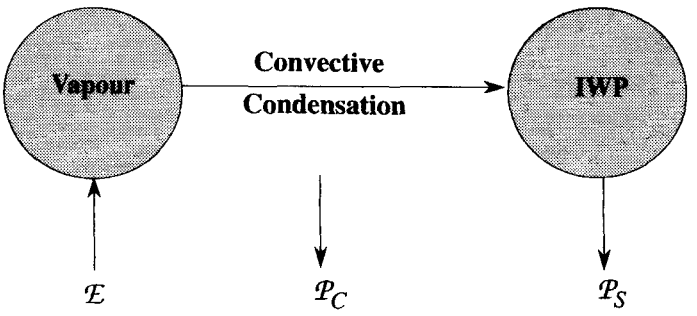

Figure 1. Illustration of the process by which cirrus ice clouds form due to convective detrainment. $\mathcal{E}$ is evaporation of sea water; $\mathcal{P}_C$ is the convective precipitation rate; *IWP* is the ice-water path; and $\mathcal{P}_S$ is the stratiform precipitation rate.

We assume that the stratiform ice cloud is produced by convective detrainment, so that the rate of ice production is proportional to the convective precipitation rate, $\mathcal{P}_C$. Cloud ice removal is due to stratiform precipitation, at rate $\mathcal{P}_S$, which in turn depends upon the amount of cloud ice. Neglecting the conversion of *IWP* to *W* by sublimation, we can write a prognostic equation of the form

$$\frac{d}{dt} IWP = \chi \mathcal{P}_C - \mathcal{P}_S, \tag{7}$$

where χ is a non-dimensional parameter. We assume that the stratiform precipitation rate satisfies

$$\mathcal{P}_S = IWP/(f t_{prec}), \tag{8}$$

and

$$\mathcal{P} = \mathcal{P}_C + \mathcal{P}_S, \tag{9}$$

where t_{prec} is the 'autoconversion' time-scale for the removal of *IWP* by stratiform precipitation and f is the fractional cloudiness. As discussed later, the fractional cloudiness is a specified parameter in this model. The cloud fraction appears in the denominator of (8) because *IWP* represents the area-averaged ice-water path, while it is the *local* ice-water path that is relevant for conversion of cloud ice to snow. Figure 1 schematically summarizes these ideas.

Using (8) and (9) in (7), we obtain

$$\begin{aligned} \frac{d}{dt} IWP &= \chi(\mathcal{P} - \mathcal{P}_S) - IWP/(f t_{prec}) \\ &= \chi(\mathcal{P} - IWP/t_{prec}) - IWP/(f t_{prec}) \\ &= \chi \mathcal{P} - (1 + \chi) IWP/(f t_{prec}). \end{aligned} \tag{10}$$

When the source and sink terms are in quasi-balance, (10) reduces to

$$IWP \cong \left(\frac{\chi f t_{prec}}{1 + \chi} \right) \mathcal{P}. \tag{11}$$

We could have written down (11) by direct assumption, i.e. a simple proportionality between the total precipitation rate and the ice-water path, but the brief derivation given

above allows some interpretation in terms of specific physical processes. Because the autoconversion time is expected to be short, of the order of 10^3 to 10^4 s (e.g. Fowler *et al.* 1996), solutions of (10) should remain close to the quasi-equilibrium solution given by (11). Note that for $f = 0$, (11) gives $IWP = 0$. Under the assumption that (11) is valid, (6) reduces to

$$\frac{dW}{dt} \cong \mathscr{E} - \mathscr{P}. \tag{12}$$

3. Hydrological cycle

The atmospheric branch of the hydrological cycle is a fundamental component of the climate system (e.g. Webster 1994), because it transport energy, controls latent-heat release and precipitation, and produces radiatively active clouds. A key goal of our study has been to construct an extremely simple model of the hydrological cycle.

We assume that the surface evaporation rate, $\mathscr{E}$, satisfies

$$\mathscr{E} = \mathscr{V}\,\mathrm{Max}[\{q_{\mathrm{sat}}(T_{\mathrm{S}}, p_{\mathrm{S}}) - q_{\mathrm{S}}\}, 0], \tag{13}$$

where $\mathscr{V}$ is a 'ventilation mass flux',

$$q_{\mathrm{sat}}(T, p) \cong \frac{\varepsilon e_0 \exp(A_e - B_e/T)}{p} \tag{14}$$

is the saturation mixing ratio at temperature T and pressure p, q_{S} is the surface air mixing ratio, and A_e and B_e are constants. Methods to determine q_{S} are discussed later.

We assume that $\mathscr{V}$ is simply proportional to a prescribed wind speed, i.e.

$$\mathscr{V} = \rho_S c_T |\mathbf{V}_{\mathrm{S}}|. \tag{15}$$

Previous studies of this type (e.g. Pierrehumbert 1995) have also relied on this assumption, but it is not very satisfactory for two reasons. First, we expect *a priori* that $\mathscr{V}$ should be related to the vigour of the hydrological cycle, i.e. that there should be some relationship between $\mathscr{V}$ and, for example, $\mathscr{P}$. Second, surface and atmospheric energy balance depend sensitively on the values of $\mathscr{V}$ prescribed. For both of these reasons, $\mathscr{V}$ should be an internal variable of the model, rather than an externally imposed parameter. This generalization is left to a future study.

We now adopt a very simple model for the cumulus clouds. We assume that the top of the convective layer, at $z = z_{\mathrm{C}}$, occurs at the neutral-buoyancy level for non-entraining parcels consisting of surface air. Moist static energy is conserved within these ascending, non-entraining parcels. Assuming that the environment at z_{C} has a saturation water vapour mixing ratio which is negligible compared to q_{S}, we can express the neutral buoyancy condition by $h_{\mathrm{S}} = s_{\mathrm{C}}$, which implies that

$$z_{\mathrm{C}} = g^{-1}\{c_p(T_{\mathrm{S}} - T_{\mathrm{C}}) + Lq_{\mathrm{S}}\}. \tag{16}$$

We assume that the tropical temperature profile of the troposphere has the form

$$T = T_{\mathrm{S}} - \Gamma_0 z - \Upsilon z^2, \tag{17}$$

where Γ_0 is the average lapse rate of the lower troposphere, and Υ is a parameter which allows the lapse rate to vary with height. Figure 2 presents the idealized temperature structure for our model. Figure 3 shows a typical sounding (solid line) over the warm pool

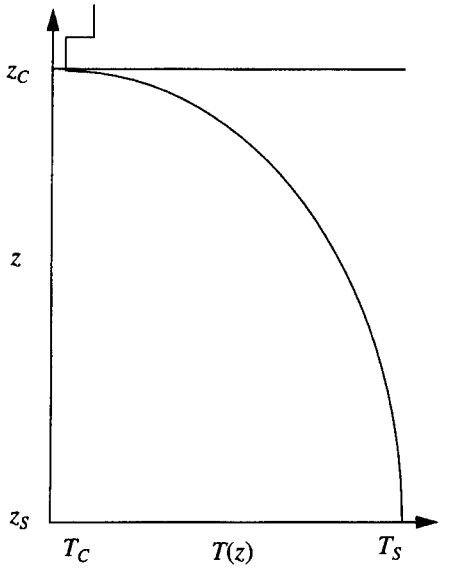

Figure 2. Schematic of the idealized tropical temperature profile, $T(z)$, in a convecting region of the tropical warm pool, where subscripts S and C indicate values at the surface and top of the convective layer respectively.

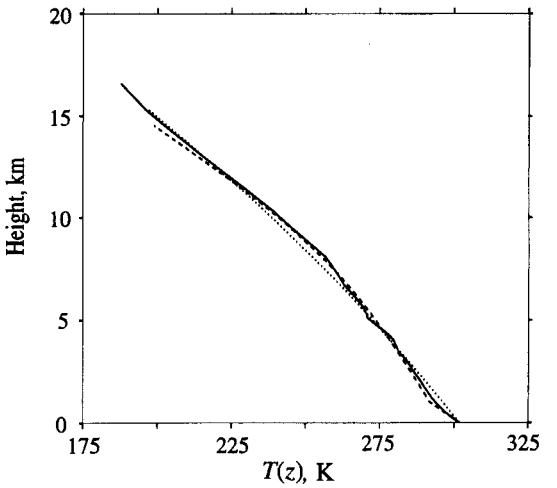

Figure 3. Observed area-mean temperature profile, $T(z)$, (solid line) for the TOGA COARE intensive flux array region. The dashed line is the moist adiabat; the dotted line is the temperature profile for the model.

from TOGA COARE* (Parsons *et al.* 1994). As is well known, the observed tropical lapse rate closely follows a moist adiabat (dashed line). Note that the lapse rate steepens near $z = 9$ km and remains steep up to the tropopause. Our method to determine Γ_0 and Υ is discussed later.

Convection plays three roles in the climate system and in our model: it releases latent heat, it leads to precipitation which dries the atmosphere, and it transports energy and water upward from the surface. Following Arakawa and Chen (1987; see also Arakawa 1993) we assume that the convective state of the tropical atmosphere can be characterized

* Tropical Ocean/Global Atmosphere Coupled Ocean-Atmosphere Response Experiment.

by a point in the $(\Gamma_n, q/q_{sat})$ plane, which is considered as a phase space. Here

$$\Gamma_n \equiv \frac{\Gamma_0 - \Gamma_{mS}}{\Gamma_d - \Gamma_{mS}}, \tag{18}$$

where $\Gamma_d = g/c_p$ is the dry adiabatic lapse rate, and Γ_{mS} is the moist adiabatic lapse rate at the surface, given by

$$\Gamma_{mS} = \Gamma_d \left\{ \frac{1 + \dfrac{Lq_{sat}(T_S, p_S)}{RT_S}}{1 + \dfrac{\varepsilon L^2 q_{sat}(T_S, p_S)}{c_p R T_S^2}} \right\} \tag{19}$$

evaluated at the surface temperature and pressure. In (19), R is the gas constant.

As discussed by Arakawa, during periods of active convection the observations tend to fall along a line which runs from the lower right to upper left in the $(\Gamma_n, q/q_{sat})$ plane; a theoretical interpretation, discussed in detail by Arakawa (1993) and Arakawa and Chen (1987), is that points along this diagonal line represent convectively neutral states toward which convection drives the system. Points below the diagonal line, e.g. drier soundings, represent convectively stable states. Points above the line represent convectively unstable states, and are forbidden in the sense that convection immediately acts to remove the instability so that it is not observed. Radiation tries to increase the lapse rate (for optically thick atmospheres), and surface evaporation tries to increase the precipitable water. Convection fights back by warming aloft and drying. Points on the stable side of the line are allowed, and are not accompanied by convection. Such points will be driven toward the unstable portion of the domain, however, by the combined effects of radiation and surface evaporation. As soon as the system tries to cross the diagonal line, convection responds to prevent it from doing so; this is a kind of convective adjustment. We therefore expect that convectively active equilibria will lie along the line, and time-dependent solutions may even stay entirely on the line. The model's position along the line can change with time as a result of a tug-of-war among convection, radiation, and surface evaporation. Hu and Randall (1994) used a very similar parametrization.

To describe this closure mathematically, we define a parameter G, which passes through zero along the diagonal line:

$$G \equiv \frac{q_s}{q_{sat}} - \frac{\Gamma_d - \Gamma_0}{\Gamma_d - \Gamma_{mS}}. \tag{20}$$

The region $G > 0$, which is 'above the line', corresponds to convective instability; and the region $G < 0$, which is 'below the line', corresponds to convective stability, i.e. conditions under which convection is suppressed. Essentially, the model allows $G \leqslant 0$, but forbids $G > 0$. When convection is active, the model 'toes the line', with

$$\frac{dG}{dt} = 0 \quad \text{and} \quad G = 0. \tag{21}$$

This simply means that during periods of active convection, the convective available potential energy (CAPE) remains close to zero. In other words, (21) is an expression of quasi-equilibrium in the spirit of Arakawa and Schubert (1974).

For $G = 0$, (20) reduces to

$$\frac{q_S}{q_{sat}} = \frac{\Gamma_d - \Gamma_0}{\Gamma_d - \Gamma_{mS}}. \tag{22}$$

This result means that, given the relative humidity at the surface, we can determine the mean lapse rate over the lower troposphere. The lapse rate Γ_0 obtained from (22) represents an approximation to the moist adiabatic lapse rate in the lower troposphere, and in fact (22) can be derived directly from a moist adiabatic assumption. Figure 3 shows that the temperature profile obtained using Γ_0 matches the observed profile and the moist adiabat rather well. The advantage of using (22) is computational simplicity; we avoid explicitly computing the temperature for multiple layers as is usually done in radiative–convective models.

To determine the total precipitation rate, we start from (3), which is the budget equation for the vertically integrated moist static energy. We approximate the moist static energy at z_C, which appears in the second term on the LHS of (3), by the dry static energy at z_C, i.e. s_C. This is justified if the upper-level water vapour mixing ratio is sufficiently small. Recall that the dry static energy at level z_C is approximately equal to the moist static energy of the surface air, i.e. $s_C = h_S$, because the convective clouds detrain at their level of neutral buoyancy, z_C. This allows us to rewrite (3) as

$$\frac{dH}{dt} - \rho_C h_S \frac{dz_C}{dt} = (-\mathcal{S}_S + \mathcal{R}_S + \mathcal{Q}_H + L\mathcal{E}) + (\mathcal{S}_C - \mathcal{R}_C). \tag{23}$$

Now we derive analytical expressions for the vertically integrated dry static energy, S, and the vertically integrated moist static energy, H. Given the assumed distribution of T with height, we can integrate the RHS of (2), as follows. First, by combining the assumed temperature distribution with hydrostatics and the ideal gas law, $p = \rho RT$, we can show that the pressure varies with height approximately according to

$$p = p_S \left(1 - \frac{z\Gamma_0}{T_S}\right)^{\frac{g}{R\Gamma_0}}. \tag{24}$$

The exponent in (21) is independent of height, but through Γ_0 it depends on T_S and W (as discussed later). We assume that p_S is a constant; Table 1 gives the values of p_S, ε, e_0, A_e, B_e, and all other numerical parameters used in this study. The temperature and pressure profiles given by (17) and (24), respectively, can be used in (2) to obtain

$$H = \frac{(\kappa + 1)T_S p_S}{\Gamma_0 \kappa + \Gamma_d} \left\{1 - \left(1 - \frac{\Gamma_0 z_C}{T_S}\right)^{\frac{g}{R\Gamma_0}+1}\right\} - z_C p_C + LW. \tag{25}$$

Because the surface pressure p_S is assumed to be constant, H is a function of T_S and W only, i.e.

$$H = H(T_S, W). \tag{26}$$

Part of the W-dependence of H comes from Γ_0 (see (37), discussed later). Because T_S and W are governed by their own prognostic equations, (26) seems to imply that there is no room to enforce (23) as an additional constraint on H. In fact, however, we *can* enforce (23), because the precipitation rate has not yet been determined. The precipitation rate must be consistent with (23), given dT_S/dt and dW/dt from (4) and (12) respectively. From (26), we can write

$$\frac{dH}{dt} = \frac{\partial H}{\partial T_S}\frac{dT_S}{dt} + \frac{\partial H}{\partial W}\frac{dW}{dt}. \tag{27}$$

Substituting for each term of (27), we obtain

$$-\mathcal{S}_S + \mathcal{R}_S + \mathcal{Q}_H + L\mathcal{E} + \mathcal{S}_C - \mathcal{R}_C + \rho_C h_S \frac{dz_C}{dt}$$

TABLE 1. DEFINITIONS, NUMERICAL VALUES, AND UNITS OF VARIOUS PARAMETERS USED IN THE MODEL

Parameter	Definition	Value and Units
p_S	Surface pressure	1000 mb
A_e	Used to compute saturation mixing ratio	21.656
B_e	Used to compute saturation mixing ratio	5418 K
ε	Ratio of molecular weights of water vapour and dry air	0.622
e_0	Used to compute saturation mixing ratio	1 mb
c_T	Transfer coefficient used to compute the evaporation rate	0.001
ρ_W	Density of liquid water	1000 kg m^{-3}
C	Heat capacity of liquid water	4200 J kg^{-1}
D	Depth of the ocean mixed layer	60 m (nominal)
σ	Stefan–Boltzman constant	5.67×10^{-8} W $m^{-2}K^{-4}$
a_0	Parameter used to relate the clear-sky downward surface long-wave radiation to the outgoing long-wave radiation	0.38532
a_1	Parameter used to relate the upward surface long-wave radiation to the outgoing long-wave radiation	1.38532
c_1	Parameter used to relate the upward surface long-wave radiation to the outgoing long-wave radiation	0.005238 m^2kg^{-1}
a_2	Parameter used to relate the clear-sky downward surface long-wave radiation to the outgoing long-wave radiation	0.9369
c_2	Parameter used to relate the clear-sky downward surface long-wave radiation to the outgoing long-wave radiation	0.0102 m^2kg^{-1}
d	Used to obtain $(\mathcal{R}_{dn})_{S,clr}$	0.25 m^2kg^{-1}
μ_0	'Average' cosine of the solar zenith angle	0.5
δp_u	Pressure depth of upper sublayer in the stratosphere	2 mb
k_l	Constant used to determine infrared optical thickness of the lower stratospheric sublayer	0.001 mb^{-1}
k_u	Constant used to determine infrared optical thickness of the upper stratospheric sublayer	0.004 mb^{-1}

$$= \frac{\partial H}{\partial T_S}\left(\frac{\mathcal{S}_S - \mathcal{R}_S - \mathcal{Q}_H - L\mathcal{E}}{\rho_W C D}\right) + \frac{\partial H}{\partial W}(\mathcal{E} - \mathcal{P}). \tag{28}$$

We can also show that z_C in our model is a function of T_S and W only. Hence, we can write a differential equation for z_C which is similar to (27), except that z_C replaces H. The details are omitted here for brevity. Using the resulting expression for dz_C/dt in (28), we find that

$$\mathcal{S}_C - \mathcal{R}_C = \Lambda_1(\mathcal{S}_S - \mathcal{R}_S - \mathcal{Q}_H - L\mathcal{E}) + \Lambda_2(\mathcal{E} - \mathcal{P}), \tag{29}$$

where, for convenience, we define

$$\Lambda_1 \equiv 1 + \frac{1}{\rho_W C D}\left(\frac{\partial H}{\partial T_S} - \rho_C h_S \frac{\partial z_C}{\partial T_S}\right), \tag{30}$$

$$\Lambda_2 \equiv \frac{\partial H}{\partial W} - \rho_C h_S \frac{\partial z_C}{\partial W}. \tag{31}$$

Solving (29) for $\mathcal{P}$, we obtain

$$\mathcal{P} = \mathcal{E} + \{\Lambda_1(\mathcal{S}_S - \mathcal{R}_S - \mathcal{Q}_H - L\mathcal{E}) + (\mathcal{R}_C - \mathcal{S}_C)\}\Lambda_2^{-1}. \tag{32}$$

In a steady state, the net energy fluxes at the surface $\mathcal{N}_S \equiv \mathcal{S}_S - \mathcal{R}_S - \mathcal{Q}_H - L\mathcal{E}$, at the top of the atmosphere (TOA) $\mathcal{N}_\infty \equiv \mathcal{S}_\infty - \mathcal{R}_\infty = \mathcal{S}_C - \mathcal{R}_C$, and across the atmosphere

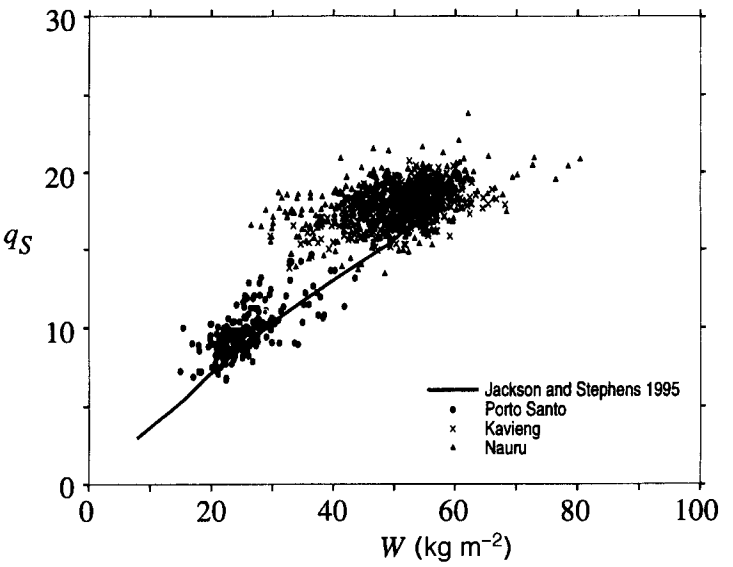

Figure 4. The relationship between the surface air mixing ratio, q_S, and precipitable water, W, as determined from radiosonde data by Liu (1986). The solid line in the figure represents the relationship derived using (33) and a relationship between sea surface temperature and W, as discussed by Jackson and Stephens (1995).

$\mathcal{N}_A \equiv \mathcal{N}_\infty - \mathcal{N}_S$, must all be zero so that (32) simply reduces to $\mathcal{P} = \mathcal{E}$. According to (32), precipitation is driven by surface evaporation, by surface warming, and by radiative energy losses at the top of the convective layer.

We assume that when convection is active the surface-air mixing ratio satisfies

$$q_S = \frac{W}{W_{max}} q_{sat}(T_S, p_S), \tag{33}$$

where W_{max} is the precipitable water that would exist if the relative humidity were 100% throughout the depth of the tropical atmosphere. The relationship (33) resembles the climatological relationship between q_S and W employed by Liu (1986) in his attempt to retrieve ocean surface energy fluxes from satellite measurements. We have performed a similar analysis using different data. The results are shown in Fig. 4. For purposes of comparison with observations, we represent q_S by the 1000 mb mixing ratio, which is conveniently available in radiosonde reports. The points in Fig. 4 were derived by matching the 1000 mb mixing ratio with the precipitable water obtained by vertically integrating the surface observations and balloon soundings taken at Kavieng and Nauru during TOGA COARE (Parsons *et al.* 1994), and at Porto Santo during the Atlantic Stratocumulus Transition Experiment (Albrecht *et al.* 1995). Satellite observations of precipitable water as a function of sea surface temperature (Jackson and Stephens 1995) were used to evaluate the assumption (33) as follows. We calculated q_{sat} from (33) and W_{max} from (19) and (36) (presented later), both as functions of observed sea surface temperature. The satellite-observed W and the derived q_{sat} and W_{max}, all corresponding to the same sea surface temperature, were then inserted into (33) to obtain the curve plotted in Fig. 4.

The fact that the line passes through the data reasonably well supports the use of (33) in our model, even though both Liu's data and our results suggest that q_S 'flattens out' at large values of W. A plausible interpretation is that over warm oceans with large W, vigorous deep convection distributes moisture through a deeper layer, effectively drying

the lower layers and moistening the air aloft. A consequence of this assumption is that the dependence of $\mathscr{E}$ on q_{sat} and q_{S} in (13) can be replaced by a dependence on W and $W_{\max}$. Since q_{S} flattens out for large values of W in nature, the evaporation rate becomes independent of W at these large values. For our model, the evaporation rate continues to decrease for a given T_{S} as W increases, even for large values of W. In nature, as W increases, the radiative effect of water vapour destabilizes the lapse rate by cooling the upper troposphere and warming the lower troposphere (Webster 1994). This destabilization can intensify convection.

Given z_{C}, the lapse rate Γ_0 and the surface temperature, we are now able to evaluate $W_{\max}$, using

$$\begin{aligned} W_{\max} &= \int_0^{z_{\mathrm{C}}} \frac{\varepsilon e_0 \exp\{A_e - B_e/T(z)\}}{p(z)} \rho(z)\, \mathrm{d}z \\ &= \frac{\varepsilon e_0}{R} \int_0^{z_{\mathrm{C}}} \frac{\exp\{A_e - B_e/T(z)\}}{T(z)}\, \mathrm{d}z \\ &\cong F(T_{\mathrm{S}})/\Gamma_0, \end{aligned} \tag{34}$$

where

$$F \equiv \frac{\varepsilon e_0 T_0}{R B_e} \exp(A_e - B_e/T_{\mathrm{S}}). \tag{35}$$

The exponential function in (34) arises from the Clausius–Clapeyron equation; the values of the constants A_e and B_e are given in Table 1. We have used (17) with $\Upsilon = 0$ to do the integral in (34). The reference temperature T_0 used in (35) is set to 300 K. In the last line of (34), we have neglected the W-dependence of $T(z)$. This approximation introduces an error of 10% or less for T_{S} in the range 290 K to 310 K.

By combining (34) with our convection closure, (22), and our surface humidity assumption, (33), we can solve for Γ_0 and $W_{\max}$ as functions of W and T_{S} only:

$$W_{\max} \cong \frac{F(T_{\mathrm{S}}) + W(\Gamma_{\mathrm{d}} - \Gamma_{\mathrm{mS}})}{\Gamma_{\mathrm{d}}}; \tag{36}$$

$$\Gamma_0 \cong \frac{\Gamma_{\mathrm{d}} F(T_{\mathrm{S}})}{F(T_{\mathrm{S}}) + W(\Gamma_{\mathrm{d}} - \Gamma_{\mathrm{mS}})}. \tag{37}$$

These equations apply only when convection is active.

4. Radiation parametrization

We now describe parametrizations for the infrared and solar radiative fluxes that appear in our prognostic equations.

(a) *Long wave*

Infrared fluxes are calculated using the approach of Stephens and Greenwald (1991), in which the clear-sky infrared emission at the surface and the clear-sky infrared emission at the TOA are related by a simple function of W, i.e.

$$(\mathscr{R}_{\mathrm{up}})_{\mathrm{S,clr}} = \sigma T_{\mathrm{S}}^4 = (a_1 + c_1 W)\mathscr{R}_{\infty,\mathrm{clr}}. \tag{38}$$

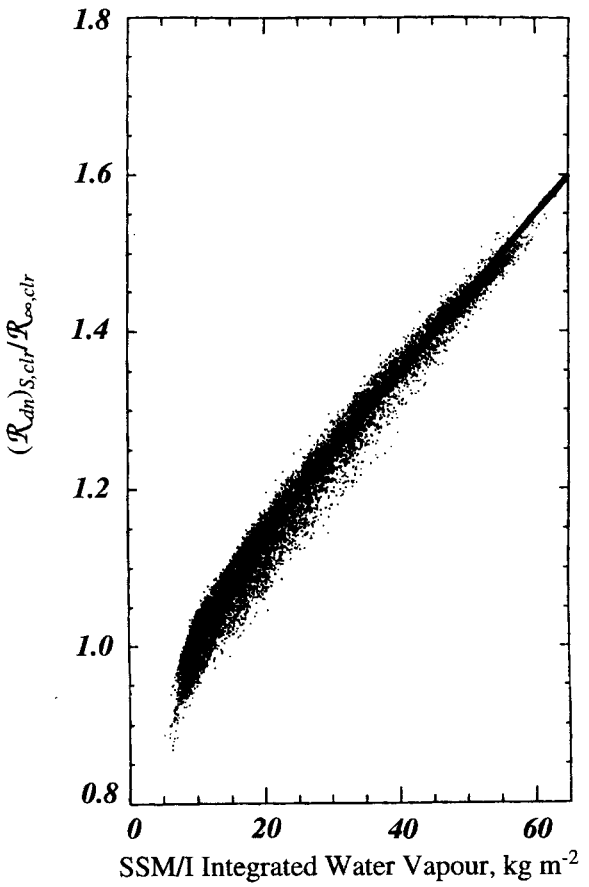

Figure 5. Results obtained with (39) in terms of the ratio of the clear-sky infrared emission at the surface, $(\mathcal{R}_{dn})_{S,clr}$ and the clear-sky infrared emission at the top of the atmosphere, $\mathcal{R}_{\infty,clr}$, compared with the simulations described in Stephens *et al.* (1994).

Here a_1 and c_1 are approximately constant and their values are given in Table 1. In addition, following Stephens *et al.* (1994), we assume that the clear-sky downward infrared radiation at the surface is related to $(\mathcal{R}_{up})_{\infty,clr}$ by a simple function of W, i.e.

$$(\mathcal{R}_{dn})_{S,clr} = [\{(a_2 - a_0) + c_2 W\}(1 - e^{-dW}) + a_0]\mathcal{R}_{\infty,clr}$$
$$= \left[\frac{\{(a_2 - a_0) + c_2 W\}(1 - e^{-dW}) + a_0}{a_1 + c_1 W}\right]\sigma T_S^4, \tag{39}$$

where a_0, a_2, and c_2 are approximately constant and are given in Table 1. Figure 5 presents results obtained with (39), expressed in terms of the ratio $(\mathcal{R}_{dn})_{S,clr}/\mathcal{R}_{\infty,clr}$, as compared with the radiative-transfer simulations described by Stephens *et al.* (1994). The assumed simple relationship between $(\mathcal{R}_{dn})_{S,clr}/\mathcal{R}_{\infty,clr}$ and W fits the simulations adequately for the purposes of this study.

By combining (38) and (39), we find that the net clear-sky long-wave radiation at the surface satisfies

$$\mathcal{R}_{S,clr} = \sigma T_S^4 \left[\frac{(a_1 - a_0 + c_1 W) - \{(a_2 - a_0) + c_2 W\}(1 - e^{-dW})}{(a_1 + c_1 W)}\right]. \tag{40}$$

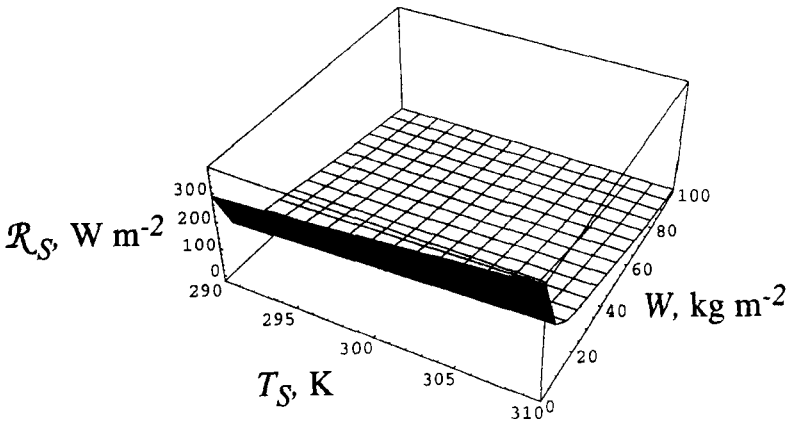

Figure 6. The net clear-sky long-wave radiation at the surface, $\mathcal{R}_S$, as a function of surface temperature, T_S and precipitable water, W.

Simply by rearranging (38), we obtain an expression for the net clear-sky long-wave radiation at the TOA. Using these simple equations, we can determine the clear-sky net long-wave radiation at the surface and the TOA in terms of T_S and W. Figure 6 shows the results for the net radiation at the surface. When W is small, $\mathcal{R}_S$ decreases sharply as W increases. Beyond $W = 40$ kg m^{-2}, T_S and W variations affect $\mathcal{R}_S$ only moderately.

With 100% cloudiness or 'overcast' skies, the upward long-wave radiation at the top of the convective layer is assumed to satisfy

$$(\mathcal{R}_{up})_{C,ovc} = (\mathcal{R}_{up})_{C,clr}(1 - \varepsilon_{cld}) + \varepsilon_{cld}\sigma T_C^4, \tag{41}$$

where ε_{cld} is the long-wave emittance of the cloud. The value for $(\mathcal{R}_{up})_{C,clr}$ can be obtained from (63) (presented later) with $\mathcal{R}_\infty = \mathcal{R}_{\infty,clr}$.

Having determined a value for $(\mathcal{R}_{up})_{C,clr}$, cloudy-sky values of z_C and T_C can be calculated by following the procedure described in section 5. The cloudy-sky values of z_C and T_C differ from their clear-sky values because clouds reduce the upward long-wave flux at level z_C thereby causing the stratosphere to cool. The overcast outgoing long-wave radiation (OLR) follows as

$$\mathcal{R}_{\infty,ovc} = (\mathcal{R})_{C,ovc}(1 - \varepsilon_l)(1 - \varepsilon_u) + (1 - \varepsilon_u)\varepsilon_l\sigma T_l^4 + \varepsilon_u\sigma T_u^4, \tag{42}$$

where ε_l and ε_u are the emissivities of the lower and upper stratospheric layers. We adopt a simplified form of the emissivity given by

$$\varepsilon_{l,u} = 1 - e^{-k_{l,u}\delta p_{l,u}}, \tag{43}$$

where $k_{l,u}$ is a constant of each layer, and $\delta p_{l,u}$ is a pressure scale. For the upper stratospheric layer, we set $\delta p_u = 2$ mb. For the lower stratospheric layer, $\delta p_l = p_C - 2$ mb, where p_C is the hydrostatic pressure that corresponds to z_C. This idealized form represents an effective emissivity in each sub-layer of the stratosphere. We estimated values of $k_{l,u}$ from more detailed radiative-transfer calculations.

The overcast net surface long-wave radiation is assumed to satisfy

$$(\mathcal{R}_S)_{ovcst} = \mathcal{R}_{S,clr} - (1 - \varepsilon_{clr})\varepsilon_{cld}\sigma T_C^4, \tag{44}$$

where ε_{clr} is the emissivity of the atmosphere below the cloud. For simplicity, we assume

$$\varepsilon_{clr} = 1 - e^{-kW}, \tag{45}$$

where k is a constant whose value is discussed below. Use of (45) in (44) gives

$$(\mathcal{R}_S)_{ovcst} = \mathcal{R}_{S,clr} - e^{-kW}\varepsilon_{cld}\sigma T_C^4. \tag{46}$$

Although the emission temperature T_C in (44) generally differs from that in (41), W is typically large enough so that the second term on the RHS of (46) is small. Observations (e.g. Stephens *et al.* 1994) show that for large W the cloud has little effect on the surface long-wave fluxes. Nevertheless, we do not neglect the second term. The value $k = 1/8\ m^2kg^{-1}$, used above, is consistent with the observations.

We use the adjective 'all-sky' to denote the actual radiation that occurs for whatever cloud fraction is specified in the model. The all-sky long-wave radiation fields are assumed to satisfy

$$\mathcal{R} = \mathcal{R}_{clr} - \mathcal{C}_{LW}, \tag{47}$$

where $\mathcal{C}_{LW}$ is the cloud long-wave forcing, which is discussed in subsection (c). Equation (47) holds for the flux of long-wave radiation at the top and bottom of the atmosphere.

(*b*) *Short wave*

The reflected overcast short-wave radiation at the TOA is assumed to satisfy

$$(\mathcal{S}_{up})_{ovcst,\infty} = (\mathcal{S}_{dn})_C\{\alpha_C + (1-\alpha_C)^2\alpha_S\mathcal{J}^2\}, \tag{48}$$

where α_C is the cloud albedo, α_S is the surface reflectivity, $\mathcal{J}$ is the transmissivity of the troposphere, and $(\mathcal{S}_{dn})_C = (1-A)\mathcal{S}_\infty$. The first term in (48) is the contribution to the upwelling flux due to direct reflection by the cloud, and the second term allows for reflection by the surface. Making $\mathcal{J}$ a function of water vapour only, we adopt a standard parametrization for water vapour absorption (Lacis and Hansen 1974). The surface reflectivity is specified to be 0.07, and cloud albedo is parametrized in terms of the *IWP*. For $\alpha_C = 0$, (48) gives the reflected clear-sky short-wave radiation at the TOA.

The downward solar radiation at the surface under overcast skies is assumed to satisfy

$$(\mathcal{S}_{dn})_{ovcst,S} = (\mathcal{S}_{dn})_C\mathcal{J}(1+\alpha_C\alpha_S\mathcal{J}^2)(1-\alpha_C). \tag{49}$$

The overcast upward solar radiation at the surface is assumed to be

$$(\mathcal{S}_{up})_{ovcst,S} = \alpha_S(\mathcal{S}_{dn})_{ovcst,S} = \alpha_S(\mathcal{S}_{dn})_C\mathcal{J}(1+\alpha_C\alpha_S\mathcal{J}^2)(1-\alpha_C). \tag{50}$$

Hence, the overcast net solar radiation at the surface is

$$\mathcal{S}_{ovcst,S} = (\mathcal{S}_{dn})_C\mathcal{J}(1+\alpha_C\alpha_S\mathcal{J}^2)(1-\alpha_C)(1-\alpha_S). \tag{51}$$

This reduces to the clear-sky net solar radiation at the surface for $\alpha_C = 0$.

As W increases from 0 to 100 kg m^{-2} in Fig. 7, the absorbed short-wave radiation at the TOA increases by less than 10 W m^{-2}; and the surface short-wave absorption increases by about 60 W m^{-2}. Hence, the model's atmosphere absorbs an increasingly greater proportion of $\mathcal{S}_{\infty,clr}$ as the column water vapour increases.

The all-sky short-wave radiation fields are assumed to satisfy

$$\mathcal{S} = \mathcal{S}_{clr} + \mathcal{C}_{SW}, \tag{52}$$

where $\mathcal{C}_{SW}$ is the short-wave cloud forcing, which is discussed in the next section. Equation (52) holds for short-wave fluxes at the TOA and surface.

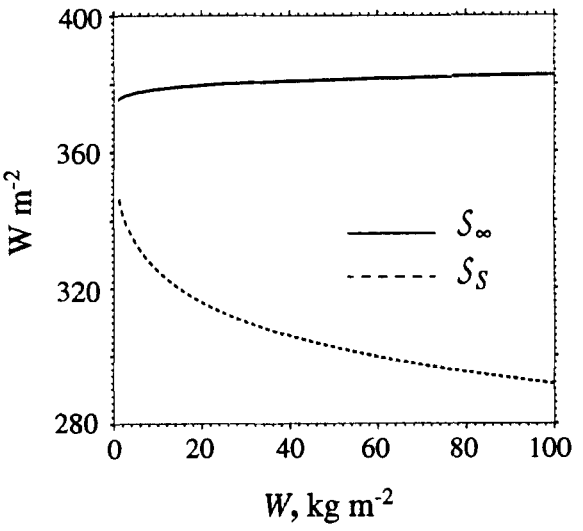

Figure 7. The net short-wave radiation at the top of the atmosphere, S_∞ (solid curve), and at the surface, S_S (dashed curve), as a function of precipitable water, W.

(c) *Cloud properties*

The short-wave and long-wave cloud radiative forcing at the surface and the TOA are assumed to satisfy:

$$(\mathscr{C}_{SW})_\infty = f\{\mathscr{S}_{ovcst,\infty} - (\mathscr{S}_\infty)_{clr}\}, \tag{53}$$

$$(\mathscr{C}_{SW})_S = f\{\mathscr{S}_{ovcst,S} - (\mathscr{S}_S)_{clr}\}, \tag{54}$$

$$(\mathscr{C}_{LW})_\infty = f\{(\mathscr{R}_\infty)_{clr} - \mathscr{R}_{ovcst,\infty}\}, \tag{55}$$

$$(\mathscr{C}_{LW})_S = f\{(\mathscr{R}_S)_{clr} - \mathscr{R}_{ovcst,S}\}. \tag{56}$$

In order to determine the long-wave and short-wave cloud radiative forcings defined above, the cloud albedo and emittance must be determined. We assume that the clouds are non-absorbing in the short wave. Since the clouds in question are produced by detrainment from deep cumuli, we suppose that they are composed of ice crystals. Following Stephens (1984), we assume that

$$\varepsilon_{cld} = 1 - e^{-k_{cld} IWP}. \tag{57}$$

The quantity $k_{cld}IWP$ is the infrared optical depth of the cloud. The 'standard value' of k_{cld} used here is 75 m^2 kg^{-1}, which is taken to be characteristic of cirrus clouds according to a gross fit of the observed albedo–emittance relationship of FIRE* data as reported by Stackhouse and Stephens (1991). For $IWP = 0.06$ kg m^{-2}, $\varepsilon_{cld} \cong 0.99$. Further increases of the IWP have little effect on the cloud emissivity, so for $IWP > 0.06$ kg m^{-2} we have emissivity *saturation*.

To determine the cloud albedo, we modify the relation obtained in a two-stream relationship (e.g. Twomey 1991), i.e.

$$\alpha_C = \frac{(\alpha_C)_{max}\tau/\mu_0}{\tau_0 + \tau/\mu_0}, \tag{58}$$

* The First International Satellite Cloud Climatology Project Regional Experiment.

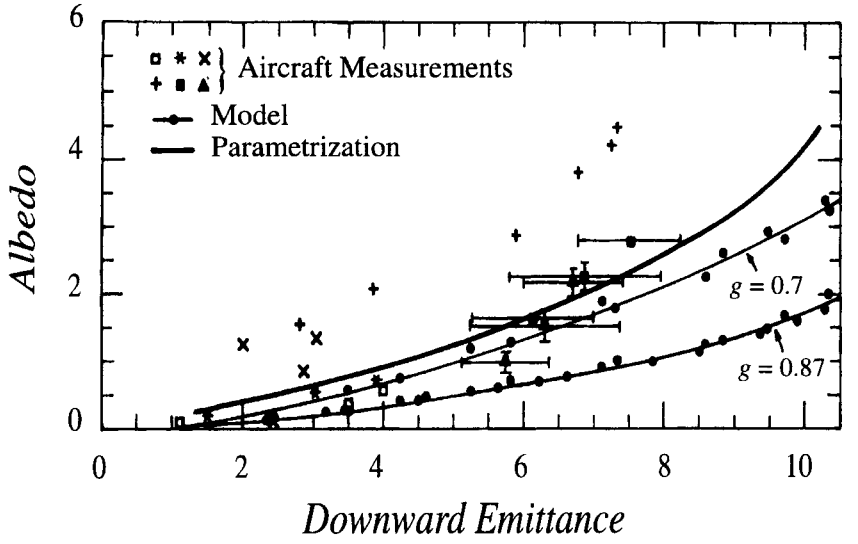

Figure 8. The albedo (×10) and downward emittance (×10) of cirrus clouds deduced from aircraft radiometric measurements summarized in Stackhouse and Stephens (1991; points) and model calculations (lines). The heavy solid curve represents the parametrization embodied in (57) through (60) with proportionality constant, $k_{cld} = 75\ m^2 kg^{-1}$. See text for details.

where $(\alpha_C)_{max}$ is a predetermined maximum possible cloud albedo, τ is the short-wave optical thickness of the cloud, μ_0 is the effective cosine of the solar zenith angle, and τ_0 is a parameter that can be related to particle-scattering asymmetry. When τ becomes large, α_C approaches its maximum value, which we set to 0.8 in this study. We assume $\mu_0 = 0.5$ throughout this study, although the form of (58) accounts for the variation of α_C with μ_0 in a realistic way. The short-wave cloud optical depth τ is parametrized according to

$$\tau = c_{cld} IWP, \tag{59}$$

where c_{cld} is a parameter which can be specified or calculated. Equation (59) can be derived using the same set of assumptions that define a linear relation between optical depth and cloud liquid-water path, as introduced by Stephens (1978).

According to (57) and (59), the infrared and short-wave optical depths of the ice clouds are proportional to *IWP*, with respective proportionality constants k_{cld} and c_{cld}. Values of these parameters can be discussed in terms of the ratio

$$c_{cld}/k_{cld} \equiv \gamma. \tag{60}$$

It is often assumed that $\gamma = 2$ (e.g. Platt 1979), although in reality the broadband value of this quantity is not well known. We show later how the solutions of the model depend on both the value of γ, and the individual values of k_{cld} and c_{cld}. The albedo–emittance relationship, with the parameter values mentioned above, is compared with the FIRE data in Fig. 8. The albedo–emittance relationship of the FIRE data is subject to considerable variability, particularly in the high-emittance region of the domain. For values of the emittance greater than 0.7, our parametrization and the radiative-transfer models significantly underestimate the cloud albedo, relative to some of the aircraft observations.

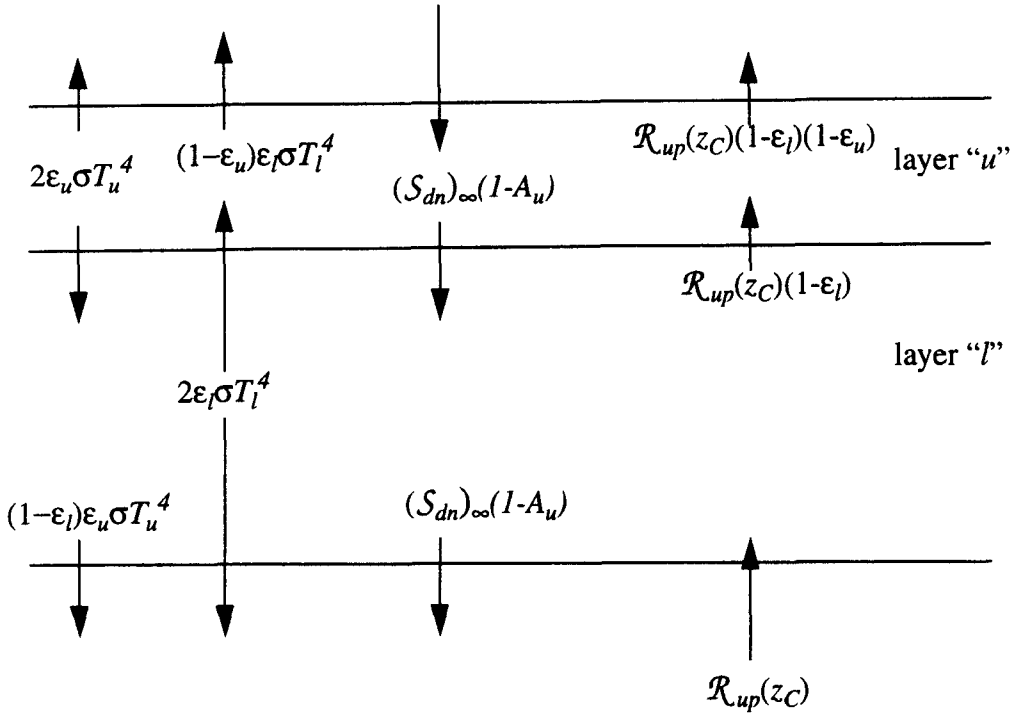

Figure 9. A schematic that describes the stratospheric radiative balance assumed in this study. See text for details of variables.

5. Solution for the Tropopause Height and Temperature

We now consider the calculation of tropopause height and temperature. We define the tropopause to be the maximum altitude reached by convecting parcels. It is also the altitude above which the atmosphere is in radiative equilibrium, rather than in radiative–convective equilibrium. Since we have assumed that the amount of CAPE in the tropical atmosphere is negligible, the buoyancy constraint would seem to provide no limitation on the depth of the convective layer. That is, convecting parcels could rise indefinitely. In nature, however, the convecting parcels become negatively buoyant as they reach the lower stratosphere. How can we model this in a simple way?

Goody and Yung (1989) described a radiative constraint imposed by the stratosphere which suffices to determine the depth of the troposphere. For a grey-absorbing atmosphere in radiative–convective equilibrium, the tropopause height is adjusted until the troposphere can deliver the radiative flux required to keep the stratosphere in radiative equilibrium. In contrast, Manabe and Strickler (1964) and Manabe and Wetherald (1967) calculated the time rate of change of temperature due to radiative heating at each level for a non-grey atmosphere, and then adjusted convectively unstable levels to an assumed lapse rate of 6.5 K km^{-1}. As the upwelling radiative fluxes across an interface (tentatively labelled as the tropopause) increase, the temperature of the layer above increases, and so the static stability increases. As the upwelling fluxes across the interface decrease, the temperature of the layer above decreases, and therefore the static stability decreases so that convective adjustment may become necessary.

These results suggest that the interactions between the stratosphere and troposphere must be modelled in order to realistically determine the tropopause height and temperature. Our model incorporates aspects of the approaches of Goody and Yung (1989) and Manabe and colleagues, plus the constraint of moist static energy conservation for convecting parcels. Given the OLR and the distribution of short-wave heating due to ozone absorption, we find values for z_C and T_C which give temperature continuity across the tropopause, are consistent with radiative equilibrium of the stratosphere, and satisfy (16). We will discuss how this is done shortly.

We model the stratosphere as two layers which are both in radiative equilibrium (Fig. 9). We assume that the heating due to ozone short-wave absorption occurs only in the upper stratospheric layer, and is balanced by thermal emission. The temperature of the lower stratosphere is assumed to be such that there is a balance between long-wave absorption and emission. Scattering in the stratosphere is neglected. For a two-layer stratosphere in radiative equilibrium, we can show that

$$\sigma T_u^4 = \frac{\mathcal{S}_\infty \mu_0 A/\varepsilon_u + (1 - \varepsilon_l/2)(\mathcal{R}_{up})_C}{2 - \varepsilon_l \varepsilon_u/2} \tag{61}$$

and

$$\sigma T_l^4 = \frac{\mathcal{S}_\infty \mu_o A/2 + (\mathcal{R}_{up})_C \left[1 + \frac{\varepsilon_u}{2}(1 - \varepsilon_l)\right]}{2 - \varepsilon_l \varepsilon_u/2}, \tag{62}$$

where A is the short-wave absorptivity of the upper stratospheric sub-layer, $\mathcal{S}_\infty$ is the mean downward flux of solar radiation at the TOA, and $(\mathcal{R}_{up})_C$ is the upward long-wave flux at level z_C. As before, subscripts u and l refer to the upper and lower sub-layers of the stratosphere. Since we have an expression for $\mathcal{R}_\infty$ (Eq. (38)), but not for $(\mathcal{R}_{up})_C$, we write $(\mathcal{R}_{up})_C$ as

$$(\mathcal{R}_{up})_C = \frac{\mathcal{R}_\infty(2 - \varepsilon_l \varepsilon_u/2) - \mathcal{S}_\infty \mu_0 A \left\{1 + \frac{\varepsilon_l}{2}(1 - \varepsilon_u)\right\}}{2 - \varepsilon_u - \varepsilon_l + \varepsilon_l \varepsilon_u/2}, \tag{63}$$

i.e. in terms of $\mathcal{R}_\infty$.

We adopt the parametrization of Lacis and Hansen (1974) for short-wave absorption due to ozone. We assume that ozone absorption occurs in the layer between 40 and 55 km. Given values of $\mathcal{R}_\infty$ and p_C, we can determine the temperature as a function of height in the stratosphere from (61) and (62), and also (63) from which we diagnose $(\mathcal{R}_{up})_C$.

The method of solution for T_C and z_C is as follows. We have three equations, (16), (17), and (62), and three unknowns, z_C, T_C, and Υ. To enforce temperature continuity across the tropopause, we set $T_C = T_l$ in (62). Given an initial guess for Υ, we compute z_C and T_C from (16) and (17), and T_l from (62). The pressure at the tropopause, p_C, which is needed to calculate the emissivity of the lower stratospheric sub-layer, is calculated from (24). If $T_C \neq T_l$, the guess for Υ is updated as a weighted average of the old value and a new value obtained from (17) with $T = T_l$. The iteration is repeated until the difference between T_C and T_l is less than 0.01 K; approximately 5 to 10 iterations suffice.

The stratospheric temperature profile depends on the upwelling long-wave flux from the troposphere in our model, just as it does for the model of Manabe and colleagues. Since T_C explicitly appears in (16), we see that the temperature of the lower stratosphere limits the height of the tropopause; as T_C increases in (16), z_C decreases if T_S and q_S remain fixed. Instead of using a prescribed lapse rate as Manabe and his colleagues did, we use our convective closure to obtain Γ_0. From (17) with $T = T_C$, $z = z_C$ and $\Upsilon = 0$, we find that $z_C = (T_S - T_C)/\Gamma_0$. Using $T_S = 303$ K, $T_C = 215$ K, and $\Gamma_0 = 6.5$ K km^{-1}, taken from

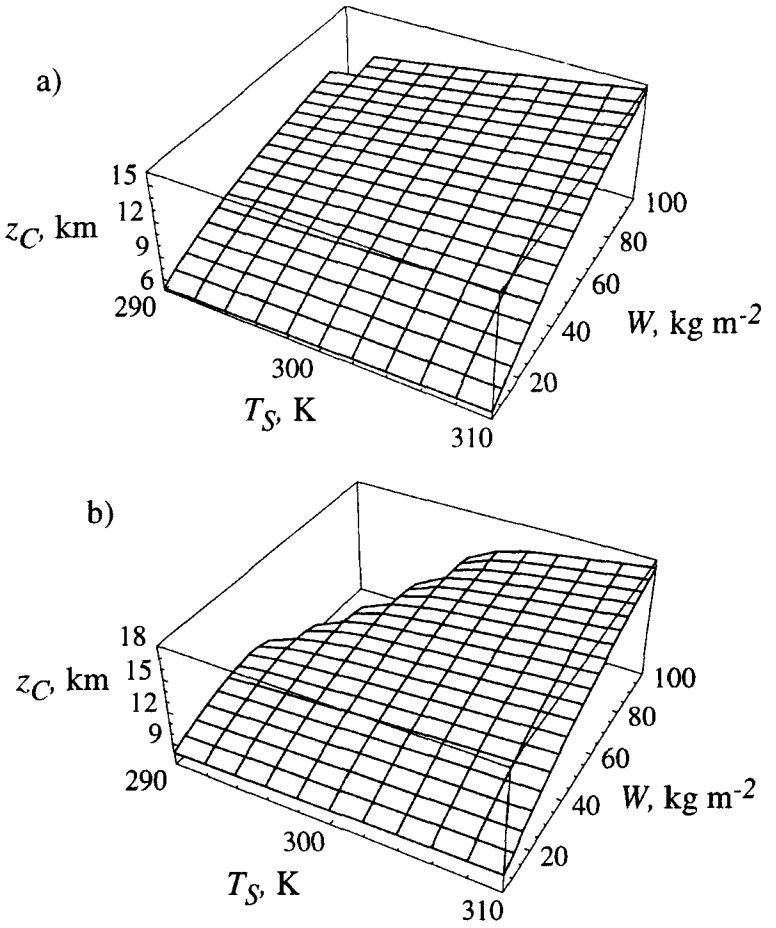

Figure 10. A contour plot of the height of the top of convection, z_C, as a function of surface temperature, T_S, and precipitable water, W, with (a) fractional cloudiness $f = 0$, (b) $f = 0.4$ with $t_{prec} = 1000$ s (see text). Values are not plotted for (T_S, W) combinations where W exceeds the maximum value possible, W_{max}, or the lapse rate becomes superadiabatic at the tropopause.

Fig. 5 in Manabe and Wetherald (1967; for their case of fixed relative humidity), we obtain $z_C = 13.5$ km. In this context, with the lapse rate fixed and constant, our results agree with those of Manabe and his colleagues. Given z_C, T_S and T_C, we can diagnose q_S from (16). Equation (33) is not needed here because the lapse rate has been prescribed. The value of q_s that we obtain implies that relative humidity $RH = 0.66$ in our model, compared to $RH = 0.77$ assumed by Manabe and Wetherald. The RH values differ because we require convecting parcels to conserve moist static energy, but Manabe and Wetherald do not. Water vapour influences their model only through radiative effects, while our model also couples the water vapour to z_C through our convection parametrization. If T_C from their Fig. 5 were smaller, e.g. $T_C = 195$ K, then both the tropopause height and relative humidity for our model would increase, e.g. $z_C = 16.6$ km and $RH = 0.81$. Thus our method probably gives better results for the tropics.

Figure 10(a) shows that if cloud-radiative effects are neglected, then z_C depends strongly on W. For fixed T_S, the upwelling flux at the tropopause increases as W decreases. As depicted in Fig. 11(a), for a given T_S, stronger long-wave upwelling causes T_C to

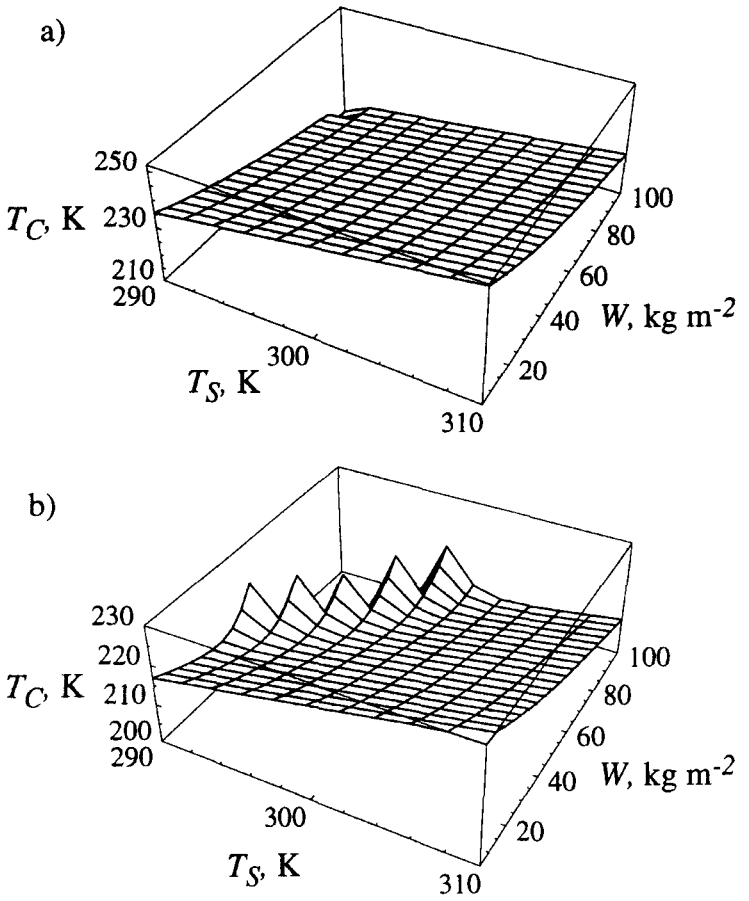

Figure 11. As Fig. 10 but for the temperature at the top of convection, T_C.

increase, which in turn causes z_C to decrease. With W fixed, z_C increases slightly with T_S. We expect z_C to rise as T_S increases if T_C remains constant. T_C increases, however, due to the increase of the upwelling long-wave flux with T_S.

6. Results

Given values of T_S and W imply an evaporation rate via (13). In equilibrium, the evaporation rate has to be balanced by the precipitation rate. Once $\mathcal{P}$ is known, the *IWP* follows from (11). From T_S, W, and *IWP*, all of the radiative fluxes can be computed. All the cloudy-sky results were generated with $t_{prec} = 5000$ s, a wind speed of 5 m s^{-1}, and $f = 0.4$ unless otherwise indicated. The upper left-hand quadrants are blacked out because W exceeds W_{max} there, which by (33) and (13) implies unphysical negative evaporation and precipitation rates.

Figures 10 and 11 compare the clear-sky values of z_C and T_C with their all-sky counterparts. Comparing Fig. 10(a) with Fig. 10(b), we see that clouds cause z_C to increase by about 2 km for fixed (T_S, W) pairs, relative to the clear-sky solutions. Of course, when cloud radiative effects are added we would expect the model to evolve to a (T_S, W) state different from that obtained with clear skies. As discussed later, increasing the fractional

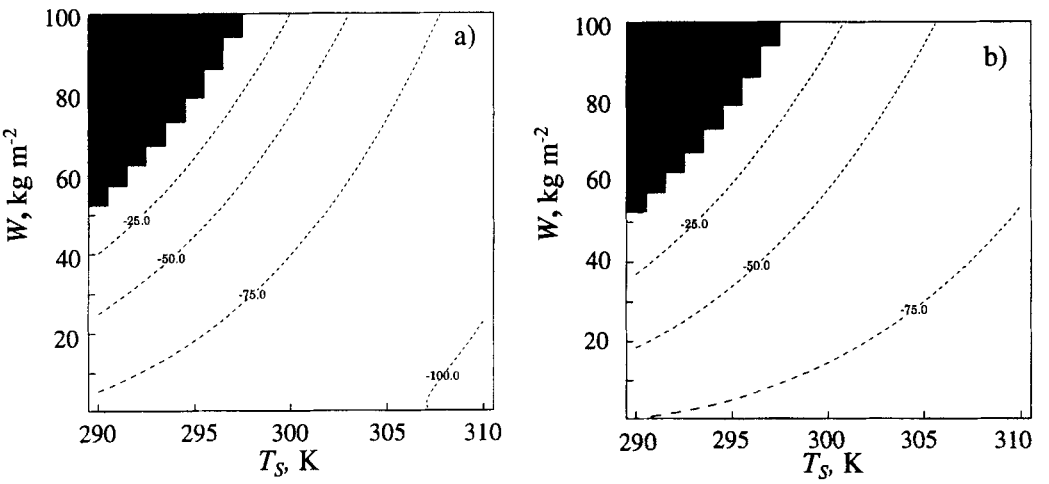

Figure 12. The short-wave cloud radiative forcing at (a) the top of the atmosphere, and (b) the surface, for the case of uniform cloudiness, as functions of precipitable water, W, and surface temperature, T_S.

cloudiness also causes z_C to increase. Figure 11 shows that clouds cause T_C to decrease by between 5 and 20 K, relative to the clear-sky results. The response of T_C to increasing T_S depends on the value of the *IWP* in a particular region of the (T_S, W) domain. In the high-W part of the domain, ε_{cld} has not yet saturated. As T_S increases, the *IWP* and, therefore, the cloud emissivity increase, which implies (from (41)) that the long-wave upwelling into the stratosphere decreases. Thus, in the high-W part of the domain, T_C must decrease as T_S increases, which is what we see in the figure. Near the blacked-out region of the domain, the *IWP* is small, so cloud radiative effects cause T_C to decrease by only 5 to 10 K. In the low-W portion of the domain, the emissivity is saturated; and as a result, the tropopause temperature follows the surface temperature.

In Fig. 12, the short-wave cloud forcing is negative for all values of T_S and W, and generally increases as the surface temperature increases and as the precipitable water decreases. As expected, the difference in the short-wave cloud forcing at the TOA and at the surface is small, approximately 15 W m^{-2}. As the surface temperature increases, more evaporation is needed to maintain surface energy balance. This requires more precipitation, which results in more *IWP* and brighter clouds. As the precipitable water increases for fixed surface temperature, the evaporation rate decreases, and, in equilibrium, so must the precipitation rate. As a result, increased precipitable water implies weaker convection and optically thinner clouds, which produce less short-wave forcing. The largest plotted values of the short-wave forcing are greater than -100 W m^{-2}, which agrees well with ERBE measurements (Harrison *et al.* 1990).

As shown in Fig. 13, the long-wave cloud forcing increases as the surface warms and as the precipitable water decreases. We expect the long-wave cloud forcing to increase as ε_{cld} increases and T_C decreases. Except for the high-W part of the domain, T_C basically increases as T_S increases and W decreases, which implies that the variations of the cloud forcing induced by ε_{cld} and T_C are opposing. Near the blacked-out region, the rapid increase of cloud emissivity as T_S increases and W decreases gives rise to a relatively strong gradient of long-wave cloud radiative forcing. Beyond this region, the cloud emissivity has saturated, and T_C increases as T_S increases and W increases, which seems to imply that the cloud radiative forcing should decrease. The clear-sky OLR increases at a slightly greater rate than the overcast-sky OLR, however, and for this reason the cloud radiative

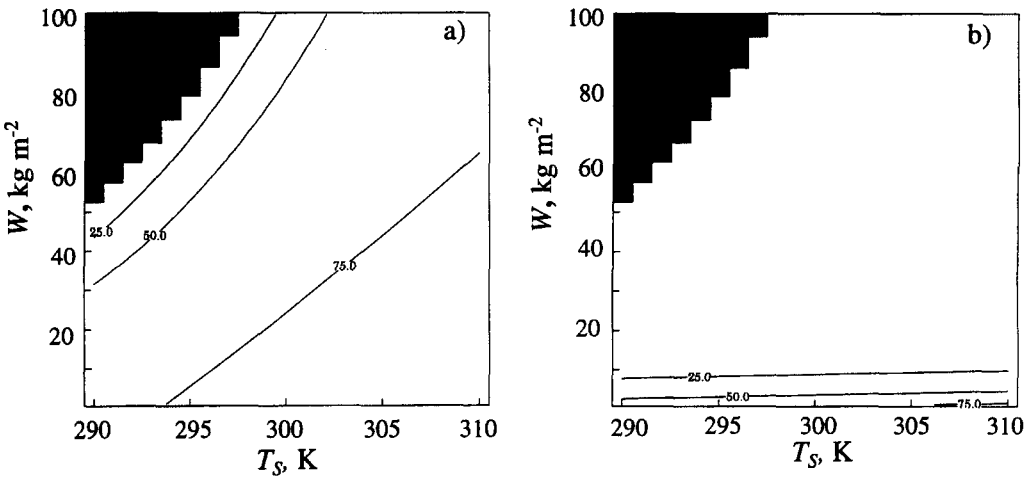

Figure 13. As Fig. 12 but for the long-wave cloud radiative forcing.

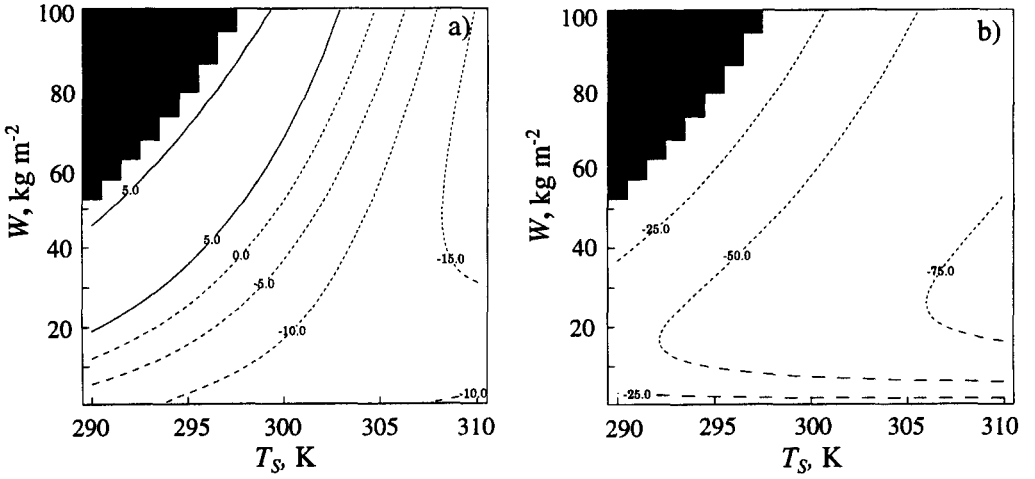

Figure 14. As Fig. 12 but for the net cloud radiative forcing. (Note the reduced contour interval in (a).)

forcing continues to gradually increase. By design, the long-wave forcing at the surface is small when the precipitable water exceeds 40 kg m^{-2}. For $W < 10$ kg m^{-2}, as the surface warms, the surface long-wave forcing increases.

The variations of the net cloud radiative forcing (Fig. 14) as a function of T_S and W are complex. The net cloud forcing at the surface is negative, as expected, if W is greater than about 5 kg m^{-2}. The TOA net cloud forcing changes from negative to positive values as the surface temperature increases and the precipitable water decreases. It varies monotonically, but interestingly it remains relatively small across the entire domain. Analyses of ERBE data show that the TOA net cloud radiative forcing in the tropics is small (Harrison *et al.* 1990). Kiehl (1994) argued that the near-cancellation of the long-wave and short-wave forcing results from the cold cloud-top emission temperatures of cumulonimbus towers in the tropics. The clouds trap energy radiated by the surface, and emit at much lower temperatures thereby reducing the OLR, relative to clear skies. In the tropics, the cloud-

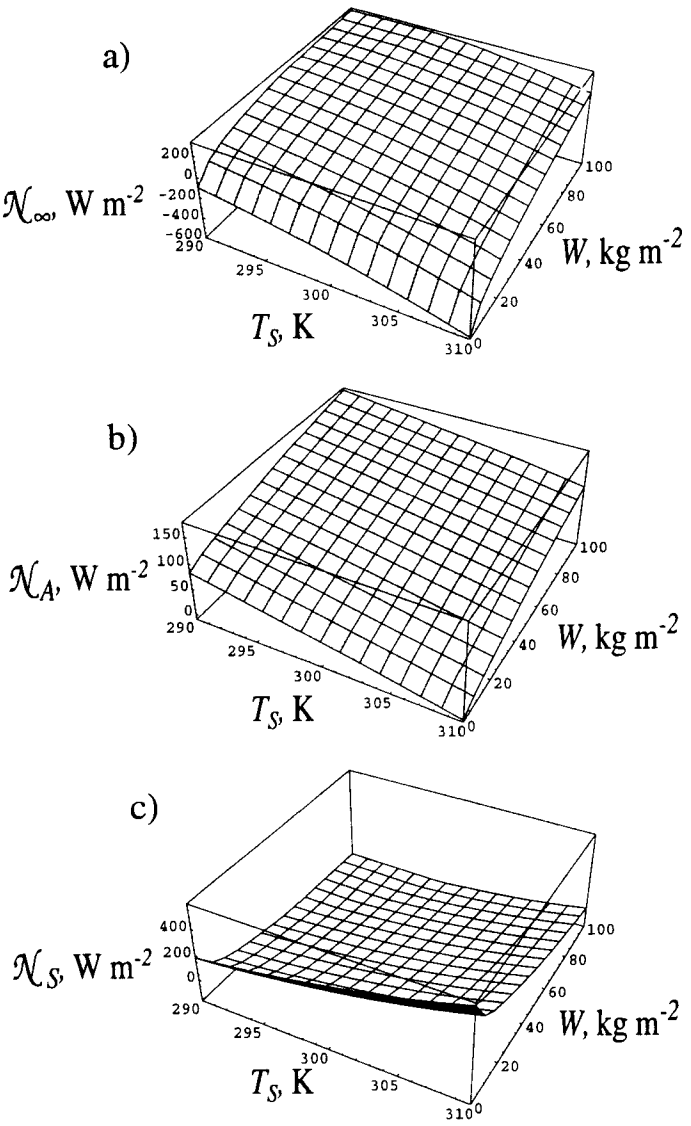

Figure 15. Clear-sky energy imbalances in terms of surface temperature, T_S, and precipitable water, W, for: (a) the top of the atmosphere, $\mathcal{N}_\infty$; (b) the atmosphere, $\mathcal{N}_A$; (c) the surface, $\mathcal{N}_S$. All are for a fixed wind speed of 5 m s^{-1}.

top emission temperatures are so low that the long-wave cloud radiative effects nearly balance the short-wave cloud-albedo effects.

The clear-sky energy imbalances at the surface, at the TOA, and across the atmosphere are shown in Fig. 15. As W increases for fixed T_S, the planet and the surface tend to gain energy, but the atmosphere tends to lose energy. Two different processes contribute to these tendencies. First, as W increases for fixed T_S, the surface evaporation rate decreases, and this reduced evaporation represents a relative gain of energy for the surface and a relative loss of energy for the atmosphere. Second, the atmosphere emits more long-wave radiation to the surface as W increases, thus cooling the atmosphere and warming the surface; at the same time, $\mathcal{R}_\infty$ decreases, although the reduction in $\mathcal{R}_\infty$ is smaller than the increase

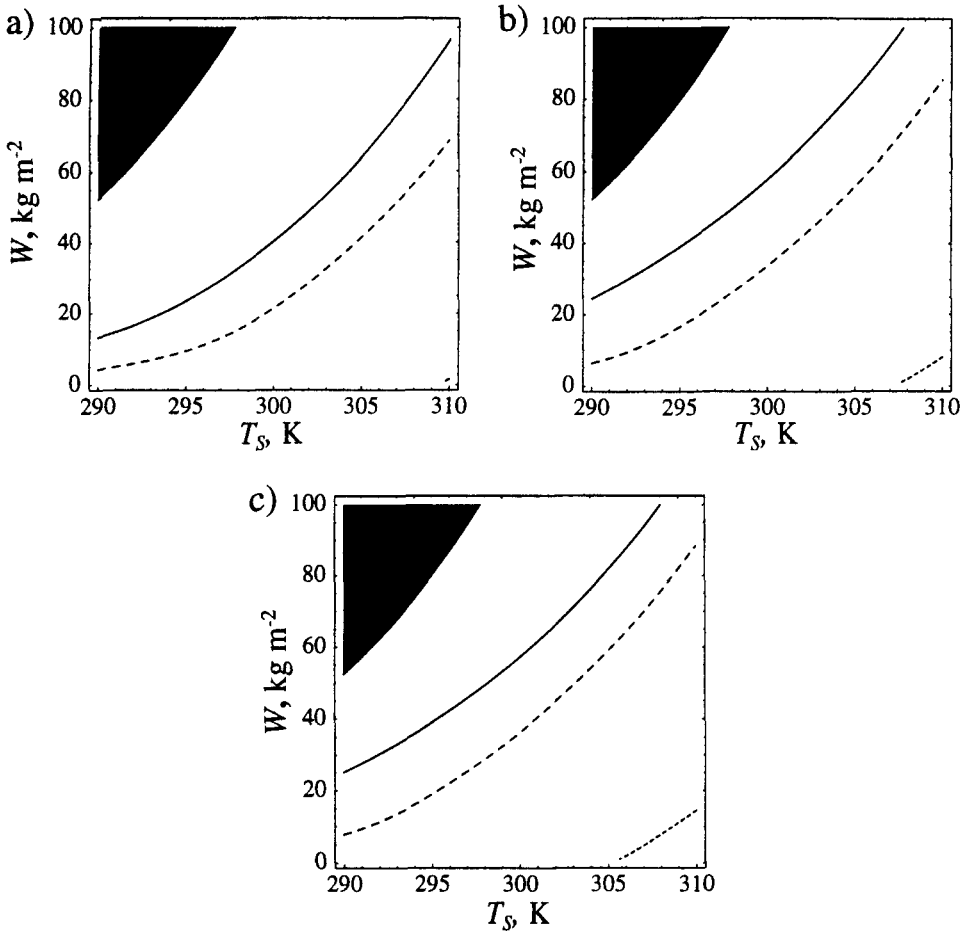

Figure 16. Contours depicting energy balance for the atmosphere (solid lines), surface (dashed lines) and planet (dotted lines) as functions of surface temperature, T_S, and precipitable water, W, for which the autoconversion timescale for the removal of the ice-water path by stratiform precipitation, t_{prec}, is as follows: (a) clear sky, $t_{prec} = 0$ s; (b) moderate cloud, $t_{prec} = 5000$ s; (c) thick cloud, $t_{prec} = 10\,000$ s. In all cases surface reflectivity $\alpha_S = 0.07$, surface wind speed $|V| = 5$ m s^{-1}, and fractional cloudiness $f = 0.4$.

in the emission to the surface (Stephens *et al.* 1994). These two effects together warm the surface and the planet, and cool the atmosphere, which is what we see in Fig. 15.

The results shown in Fig. 16(a) are the same as those shown in Fig. 15, except that only the zero contours of the imbalances are plotted. We consider $\alpha_S = 0.07$ and $|V_S| = 5$ m s^{-1}. The black region in the upper left portion of each panel indicates where the 'Max{}' function has been triggered in the computation of the evaporation rate, i.e. $W > W_{max}$. Solutions in the black region are, therefore, physically meaningless, and so are not plotted. Figure 16 depicts three curves: along the solid curve, the atmosphere is in energy balance; along the dashed curve, the surface is in energy balance; along the dotted curve, the net radiation at the TOA is zero. An equilibrium would exist if the three curves intersected, which they do not in this case.

To the right of their respective zero contours in Fig. 16(a), the planet and surface lose energy, while the atmosphere gains energy. For the surface and the atmosphere, the values of W required for energy balance of each system increase as T_S increases, but at somewhat

different rates. For example, as the surface temperature increases, more water vapour is needed to limit the rate at which the surface cools radiatively and by evaporation. Within the range plotted here, TOA radiation balance occurs only at very high T_S and low W. The TOA radiation balance depends, in the absence of clouds, on T_S, W, and α_S only. The dotted line in Fig. 16 is not affected by changing the wind speed.

If we regard the surface temperature as given, then the solid curve in Fig. 16(a), which indicates atmospheric energy balance, represents equilibria of the model. These equilibria would correspond to atmospheric GCM-simulated climates obtained with fixed sea surface temperatures; the literature is full of such studies. For a sea surface temperature of 300 K and a wind speed of 5 m s^{-1}, the model atmosphere is in equilibrium with precipitable water close to 40 kg m^{-2}, which is quite realistic for the tropics.

Figures 16(b) and (c) show the zero-energy-balance contours obtained with $t_{prec} =$ 5000 s (moderate cloud) and 10 000 s (thick cloud). No equilibria occur for either value of t_{prec}. As the clouds thicken, more column water vapour is required to balance the energy budget at all three levels, particularly at the TOA. Note the similarity between the clear-sky energy balances at the surface and across the atmosphere and those obtained with moderate and thick cloud. From Fig. 12, we see that the cloud short-wave forcing at the surface is nearly constant along the zero-balance contours for the surface in Figs. 16(b) and (c). Since long-wave cloud radiative forcing contributes little to the surface energy balance, the clear-sky surface energy balance dictates the shape of the all-sky zero-balance contour at the surface. If we subtract the net cloud radiative forcing field at the TOA from that at the surface, we can show that the same conclusion holds approximately for the energy balance across the atmosphere.

We computed the energy budgets for various combinations of cloud fractions and wind speeds. The model is in equilibrium for $t_{prec} = 15\,000$ s, a very weak prescribed wind speed of 1 m s^{-1}, $T_S = 313$ K and $W = 12$ kg m^{-2}. Since energy balance must be achieved locally, this warm, dry equilibrium does not seem altogether unreasonable. The low column water vapour makes the atmosphere's greenhouse effect small, so that radiation is very efficient at transporting heat to space.

The equilibrium solution discussed above is unstable in a coupled model, as can easily be demonstrated by time integration of the equations. Figure 17 schematically illustrates the mechanism of the instability. If we perturb the equilibrium by increasing the sea surface temperature, the atmosphere will quickly regain equilibrium, long before the ocean can cool off again, so that the model will find itself along the solid line (which denotes atmospheric equilibrium). As we move up the solid line, the surface energy imbalance becomes positive, i.e. the surface tends to warm. The initial positive perturbation of the sea surface temperature is thus amplified, and the system moves away from equilibrium; in other words, instability occurs. This happens whenever the solid line is to the left of the dashed line on the 'warm' side of equilibrium, as it is in the upper panel of Fig. 17.

When the wind speed is increased to 5 m s^{-1}, the amount of water vapour increases and the greenhouse effect becomes too strong for the system to reach equilibrium. Results from time integrations of the model provide a basis for an interpretation of the model's inability to reach equilibrium of the ocean–atmosphere system. As the surface warms, the precipitable water increases and leads to more surface warming. The evaporative cooling cannot balance the radiative heating and the surface temperature increases without bound. We identify this condition as a 'runaway greenhouse' (Ingersoll 1969). Although our model produces a warm and dry equilibrium, it is unstable, so our results tend to confirm those of Pierrehumbert (1995); in order to find an equilibrium that resembles the observed climate, a second mostly non-convecting, low-water-vapour region is needed to receive and radiate to space the excess energy of the convecting region.

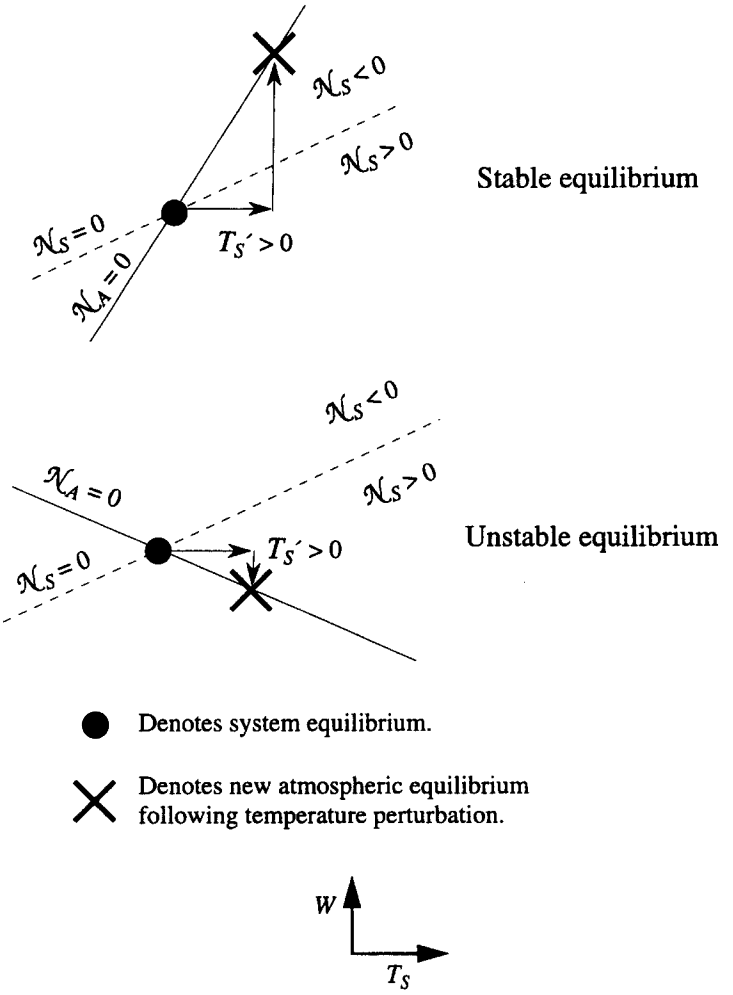

Figure 17. Schematic illustrating unstable and stable equilibria of the earth–atmosphere system. See text for explanation.

7. Equilibria with prescribed lateral energy and moisture transports

We have argued above that lateral energy and moisture transports are required to account for the observed mean climate of the deep tropics. As shown schematically in Fig. 18, the radiative–convective equilibrium state is quite different from the observed state, in terms of lateral moisture and energy transports. To show how the model responds to realistic transports, we alter its hydrological and energy budgets to include prescribed transports.

With prescribed transports, the atmospheric moisture budget, the atmospheric moist static energy budget, and the surface energy budget satisfy

$$\frac{dW}{dt} = \mathscr{E} - \mathscr{P} + \mathscr{F}_W, \tag{64}$$

$$\frac{dH}{dt} = \mathscr{N}_\infty - \mathscr{N}_S + \rho_C h_C \frac{dz_C}{dt} + \mathscr{F}_E, \tag{65}$$

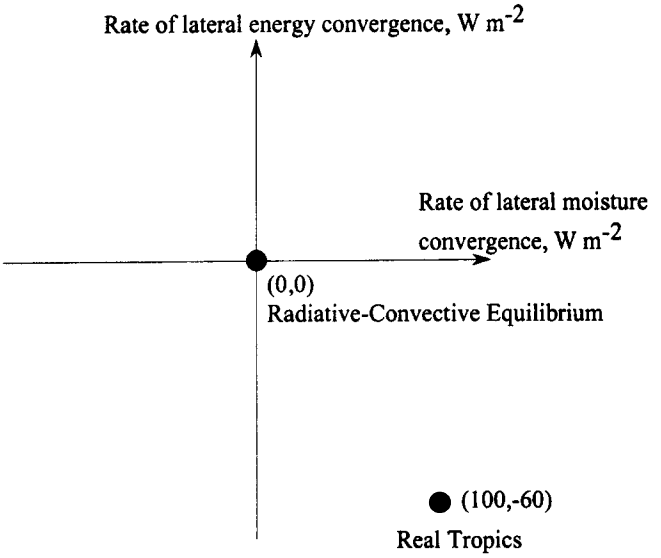

Figure 18. Schematic phase diagram showing the lateral convergences of moisture and energy in the tropics. See text for explanation.

$$\rho_w C D \frac{dT_S}{dt} = \mathcal{N}_S + \mathcal{F}_O, \tag{66}$$

respectively. Here, $\mathcal{F}_W$ is the flux convergence of moisture in the atmosphere, $\mathcal{F}_E$ is the flux convergence of energy in the atmosphere, and $\mathcal{F}_O$ is the flux convergence of energy in the ocean's mixed layer. Including these additional terms in our equation for the precipitation rate, we obtain

$$\mathcal{P} = \mathcal{E} + \mathcal{F}_W + \{\Lambda_1 \mathcal{N}_S + (\Lambda_1 - 1)\mathcal{F}_O - \mathcal{N}_\infty - \mathcal{F}_E\}\Lambda_2^{-1}. \tag{67}$$

Equation (67) implies that the precipitation rate increases as the evaporation rate increases, the moisture convergence increases, and the energy convergences in the atmosphere and ocean decrease.

In equilibrium, $\mathcal{P} = \mathcal{E} + \mathcal{F}_W$, $\mathcal{N}_S + \mathcal{F}_O = 0$, and $\mathcal{N}_\infty - \mathcal{N}_S + \mathcal{F}_E = 0$. We have prescribed the moisture and energy transports as $\mathcal{F}_W = 100$ W m^{-2} (Trenberth and Guillemot 1995) and $\mathcal{F}_E = -60$ W m^{-2} (Ramanathan and Collins 1991), respectively. We set $\mathcal{F}_O = 0$ for simplicity.

The equilibrium results are presented in Fig. 19 for $\gamma = 2$ (upper panels), for $\gamma = 3$ (lower panels), and for a wind speed of 5 m s^{-1} in both cases. If the model did not reach equilibrium for a given f and t_{prec} combination, results were not plotted. In contrast to the radiative–convective simulations, the model now can find equilibria for a range of f and t_{prec}. In general, T_S and W decrease as t_{prec} increases, for fixed f. For fixed t_{prec}, minima of both fields are evident near $f = 0.45$. For $\gamma = 2$, T_S lies between 295 and 302 K, while W ranges between 35 and 50 kg m^{-2}. With $\gamma = 3$, values for both fields are somewhat lower. Given the simplicity of the model, these values seem sufficiently realistic.

The model reaches equilibrium for a greater range of f and t_{prec} combinations with $\gamma = 3$ than with $\gamma = 2$. As suggested by Fig. 14 and Fig. 20, the net TOA cloud forcing becomes more negative as γ increases from two to three. Consequently, with larger γ, the net radiative flux at the TOA balances the prescribed lateral energy transport over a wider

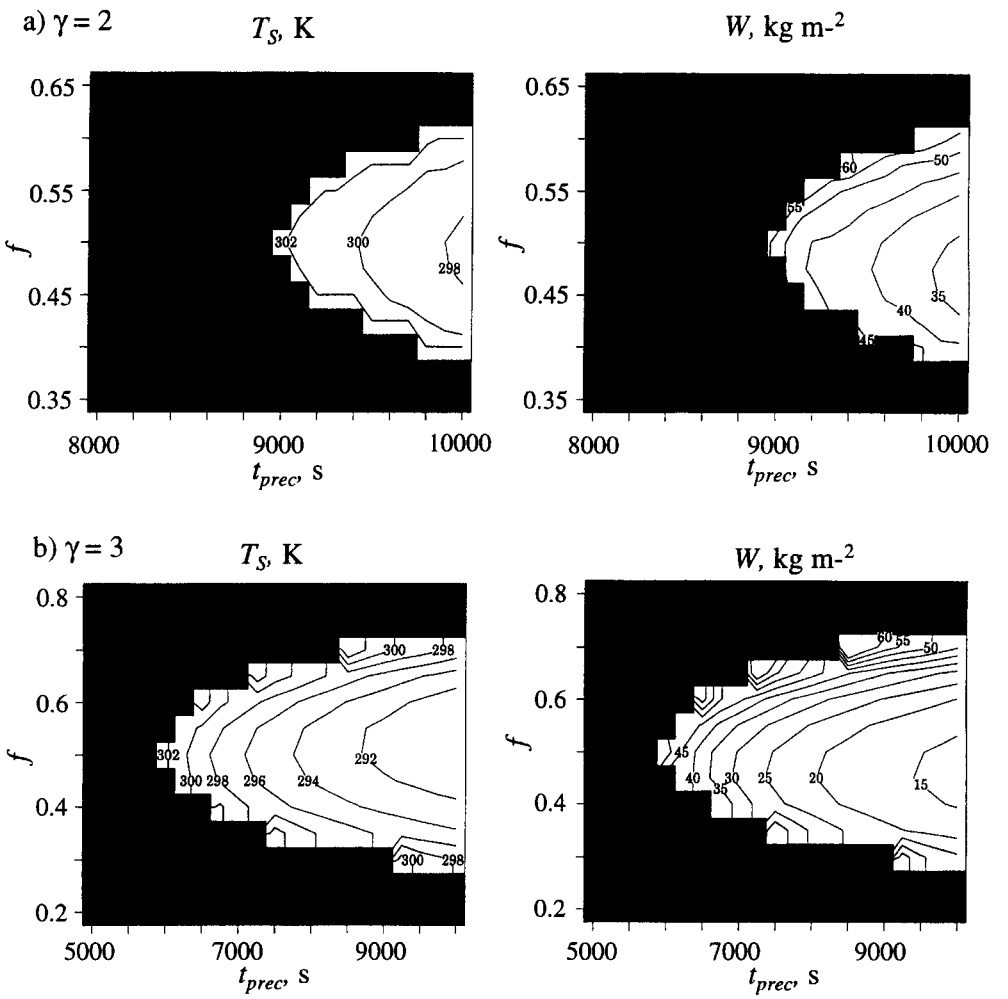

Figure 19. Equilibrium solutions with prescribed lateral energy and moisture transports are presented. The plots show surface temperature, T_S, and precipitable water, W, as functions of the autoconversion time-scale for the removal of the ice-water path by stratiform precipitation, t_{prec} and fractional cloudiness f, for: (a) ratio of short-wave to long-wave optical depths (see (60)) $\gamma = 2$; and (b) $\gamma = 3$. Values are not plotted for (T_S, W) combinations for which no solutions were found.

range of f and t_{prec} combinations. In overlapping regions in which the model reaches equilibrium for both values of γ, the equilibrium values of T_S and W are smaller for $\gamma = 3$ than for $\gamma = 2$. With relatively brighter clouds for $\gamma = 3$, the lower $\mathcal{R}_\infty$ that results from a lower surface temperature is sufficient for the net radiation at the TOA to balance the prescribed lateral energy transport. Although brighter clouds reduce the short-wave radiation absorbed by the ocean, the lower surface temperature tends to reduce the upward long-wave radiation and evaporation. In order to cool the surface sufficiently, the model decreases W which leads to a larger evaporation rate and a smaller downward long-wave flux at the surface.

To understand this behaviour of the model for a given value of γ, consider Fig. 21 which shows the net atmospheric radiative cooling (ARC) as a function of t_{prec} and f,

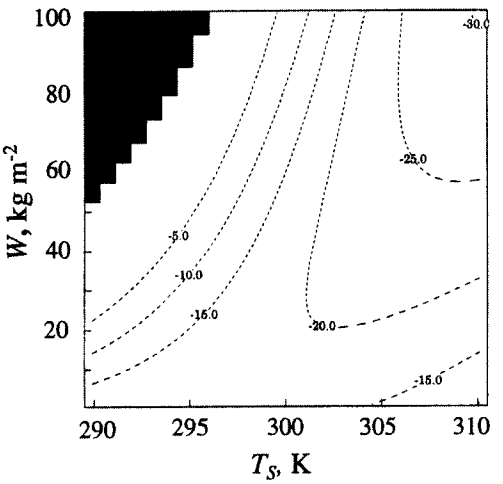

Figure 20. Contour plot of net cloud radiative forcing at the top of atmosphere for a ratio of short-wave to long-wave optical depths (see (60)) $\gamma = 3$.

where

$$ARC = \mathcal{S}_S - \mathcal{S}_\infty + \mathcal{R}_\infty - \mathcal{R}_S. \tag{68}$$

Holding f fixed, the ARC decreases as t_{prec} increases. From (11), the IWP is proportional to both $\mathcal{P}$ and t_{prec}, whose changes oppose each other. With lateral flux convergences included in these simulations, $L\mathcal{P}$ no longer equals the ARC, although $\mathcal{P}$ still decreases as the ARC decreases. The net effect is that the IWP increases slightly across the range of t_{prec} for which equilibria occur. Since the IWP ranges between 0.25 and 0.35 kg m^{-2}, the cloud emissivity has become saturated and the IWP increase causes the clouds to brighten without affecting the OLR. As a result, the surface temperature must fall in order to reduce the OLR and maintain energy balance at the TOA. Since $\mathcal{P} = \mathcal{E} + \mathcal{F}_W$ in equilibrium, and $\mathcal{F}_W$ is fixed, changes of the evaporation rate follow those of the ARC. Hence, the evaporation rate decreases as t_{prec} increases, which implies from (13) that W/W_{max} increases as t_{prec} increases. The surface temperature decrease implies that W_{max} must decrease, and thus W must fall rather strongly in order for the evaporation rate to decrease. Despite the lower surface temperature, the net upward long-wave radiation actually increases, because the decrease in W makes the atmosphere more transparent to long-wave radiation. Hence, the increase in $\mathcal{R}_S$ is actually the main contributor to the decrease in the ARC.

For fixed t_{prec}, the minima of T_S and W for $f = 0.45$ are also quite interesting. With f relatively large the ARC is weak, which implies that the latent heating of the atmosphere is relatively weak. In order to balance the hydrologic cycle, the evaporation rate must decrease. The model accomplishes this by increasing W to approximately 40 kg m^{-2}, which makes the atmosphere more opaque to long-wave radiation, and therefore causes T_S to increase. With a higher W, the surface must radiate at a higher temperature in order for the TOA net radiation to achieve the proper balance. In the middle range of the cloud fractions, the ARC is stronger and $\mathcal{P}$ is higher. The model adjusts by decreasing W. With smaller W, the surface evaporative and radiative cooling increase and cause the surface temperature to decrease. At the lowest cloud fractions, the ARC is strong and $\mathcal{P}$ is large. Nevertheless, the short-wave cloud radiative forcing is relatively weak because the cloud fraction is small. Correspondingly, T_S increases.

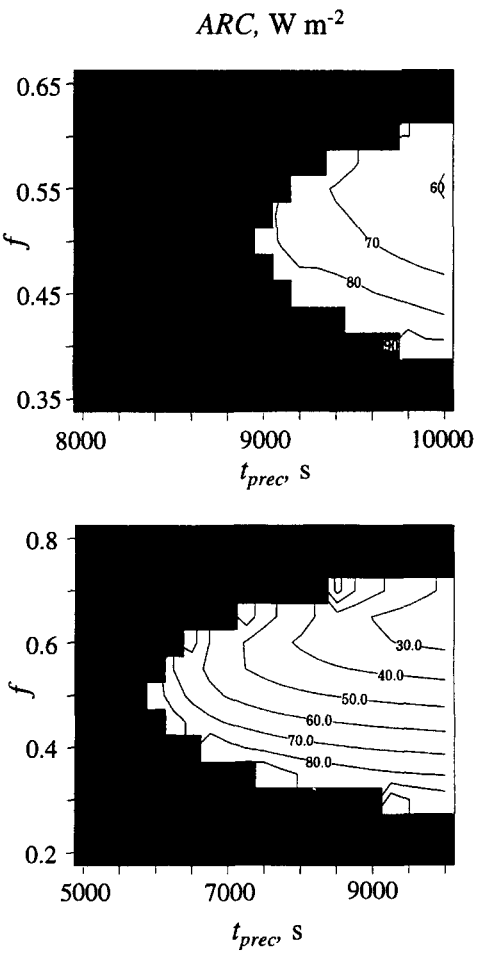

Figure 21. Contour plots of *ARC* (atmospheric radiative cooling) for a ratio of short-wave to long-wave optical depths (see (60)) $\gamma = 2$ (top) and $\gamma = 3$ (bottom), as a function of the autoconversion time-scale for the removal of the ice-water path by stratiform precipitation. Values are not plotted for combinations of surface temperature and precipitable water for which no solutions were found.

8. Summary and conclusions

We have presented an idealized but physically based radiative–convective model with a hydrological cycle. The prognostic variables of the model are the precipitable water and the sea surface temperature. Cumulus convection is parametrized using a very simple closure assumption suggested by the work of Arakawa and Chen (1987) and Arakawa (1993). Surface evaporation is parametrized using a bulk aerodynamic formula, in which the surface wind speed is prescribed. Clear-sky radiative transfer is parametrized using simple methods based on the work of Stephens *et al.* (1994) and others cited in the text. The atmospheric lapse rate is also determined by the model.

Our clear-sky results show that realistic quasi-tropical equilibria occur for realistic (warm) prescribed sea surface temperatures and surface wind speeds, but realistic clear-sky equilibria of the tropical atmosphere–ocean system do not occur. When the surface temperature is allowed to vary, the model runs away. This imbalance indicates the need for lateral energy transports and/or radiatively active clouds.

We have shown that simulating realistic cloud radiative effects allows the model to reach very warm, dry equilibrium. Because the radiative–convective equilibrium solutions do not resemble the observed tropical climate, we tested prescribed realistic lateral energy and moisture transports. With tropical moisture and energy convergence specified as 100 W m^{-2} and -60 W m^{-2}, respectively, and for $t_{prec} = 9500$ s, $f = 0.5$, $\gamma = 2$, and a wind speed of 5 m s^{-1}, the equilibrium solution occurs for $T_S = 300$ K and $W = 40$ kg m^{-2}, which are quite reasonable.

We also found that the tropopause height and temperature are sensitive to cloud radiative effects. The decreased upward long-wave flux that results when cloud radiative effects are included causes the tropopause temperature to fall as cloud optical thickness or cloud fraction increase. Reinforcing this trend is the concurrent increase of column water vapour, which reduces the clear-sky contribution to the OLR.

As either the cloud optical thickness or cloud fraction increase, the short-wave radiation absorbed by the surface decreases. To reach energy balance, the column water vapour must increase in order to reduce surface evaporative and radiative cooling. The buoyancy condition for non-entraining parcels, (16), dictates that for fixed T_S, the tropopause height must increase as the tropopause temperature decreases and the surface relative humidity increases, both of which occur as the cloud optical depth and cloud fraction increase. The cloud fraction strongly affects the height and temperature of the tropopause because it affects the long-wave radiation upwelling into the stratosphere. The effects of cloud optical thickness are self limiting, however, because the emissivity saturates as the *IWP* increases beyond 0.1 kg m^{-2}.

The key sensitivities in this model are to the prescribed wind speed, to γ, and to the values of c_{cld} and k_{cld}, and t_{prec}. Equilibrium solutions with prescribed lateral energy and moisture transports showed a marked sensitivity to γ, the ratio of short-wave to long-wave optical depths, and to f. Work is underway to add a 'radiator fin' and model-predicted surface wind speeds.

Acknowledgements

We thank Paul Ciesielski and John Kleist for providing and advising us on the TOGA COARE and ASTEX datasets, respectively. We thank Darren Jackson for making available his satellite-derived water vapour–sea surface temperature relationships. We also thank the two reviewers for their insightful comments and helpful suggestions. This project has been supported by the National Aeronautics and Space Administration under Grants NAG5-1058 and NAG8-981, and by the National Science Foundation under Grants ATM-8907414 and ATM-0100795, all to Colorado State University.

References

Albrecht, B. A., Bretherton, C. S., Johnson, D., Schubert, W. H. and Frisch, A. S. 1995 The Atlantic Stratocumulus Transition Experiment—ASTEX. *Bull. Am. Meteorol. Soc.*, **76,** 889–904

Arakawa, A. 1993 Closure assumptions in the cumulus parameterization problem. In *The representation of culumus convection in numerical models.* Eds. K. Emanuel and D. Raymond. American Meteorological Society, Boston, USA

Arakawa, A. and Chen, J.-M. 1987 Closure assumptions in the cumulus parameterization problem. In *Short and medium range numerical weather prediction.* WMO/IUGG Symposium on Numerical Weather Prediction, Tokyo, 4–8 August 1986. Special Vol., *J. Meteorol. Soc. Jpn.*

Arakawa, A. and Schubert, W. H. 1974 Interaction of a cumulus cloud ensemble with the large-scale environment. Part I. *J. Atmos. Sci.*, **31,** 674–701

Betts, A. K. and Ridgway, W.	1989	Climatic equilibrium of the atmospheric convective boundary layer over a tropical ocean. *J. Atmos. Sci.*, **46,** 2621–2641
Emanuel, K. A.	1991	A scheme for representing cumulus convection in large-scale models. *J. Atmos. Sci.*, **48,** 1763–1775
Fowler, L. D., Randall, D. A. and Rutledge, S. A.	1996	Liquid and ice cloud microphysics in the CSU General Circulation Model: Part I. Model description and simulated microphysical processes. *J. Climate*, **9,** 489–529
Goody, R. M. and Yung, Y. L.	1989	*Atmospheric radiation theoretical basis*, 2nd Ed. Oxford University Press, New York
Harrison, E. F., Minnis, P., Barkstrom, B. R., Ramanathan, V., Cess, R. D. and Gibson, G. G.	1990	Seasonal variation of the Earth Radiation Budget Experiment. *J. Geophys. Res.*, **95,** 18687–18703
Hu, Q. and Randall, D. A.	1995	Low-frequency oscillations in radiative–convective systems. Part II: An idealized model. *J. Atmos. Sci.*, **52,** 478–490
Ingersoll, A. P.	1969	The runaway greenhouse: A history of water on Venus. *J. Atmos. Sci.*, **26,** 1191–1198
Jackson, D. L. and Stephens, G. L.	1995	A study of SSM/I derived precipitable water over the global oceans. *J. Climate*, **8,** 2025–2038
Kiehl, J. T.	1994	On the observed near cancellation between longwave and shortwave cloud forcing in tropical regions. *J. Climate*, **7,** 559–565
Lacis, A. and Hansen, J. E.	1974	A parameterization for the absorption of solar radiation in the earth's atmosphere. *J. Atmos. Sci.*, **31,** 118–133
Lau, W. K.-M., Sui, C.-H., Chou, M.-D. and Tao, W.-K.	1994	An inquiry into the cirrus cloud thermostat effect for tropical sea surface temperatures. *Geophys. Res. Lett.*, **21,** 1157–1160
Liu, W. T.	1986	Statistical relation between monthly mean precipitable water and surface-level humidity over global oceans. *Mon. Weather Rev.*, **114,** 1591–1602
Manabe, S. and Strickler, R. F.	1964	Thermal equilibrium of the atmosphere with a convective adjustment. *J. Atmos. Sci.*, **21,** 361–385
Manabe, S. and Wetherald, R. T.	1967	Thermal equilibrium of the atmosphere with a given distribution of relative humidity. *J. Atmos. Sci.*, **24,** 241–259
North, G. R.	1975	Theory of energy balance climate models. *J. Atmos. Sci.*, **32,** 2033–2043
Parsons, D., Dabberdt, W., Cole, H., Hock, T., Martin, C., Barrett, A.-L., Miller, E., Spowart, M., Howard, M., Ecklund, W., Carter, D., Gage, K. and Wilson, J.	1994	The integrated sounding system: description and preliminary observations from TOGA COARE. *Bull. Am. Meteorol. Soc.*, **75,** 553–567
Pierrehumbert, R. T.	1995	Thermostats, radiator fins, and the runaway greenhouse. *J. Atmos. Sci.*, **52,** 1784–1806
Platt, C. M. R.	1979	Remote sounding of high clouds: I. Calculation of visible and infrared optical properties from lidar and radiometer measurements. *J. Appl. Meteorol.*, **18,** 1130–1143
Ramanathan, V. and Coakley, Jr. J. A.	1978	Climate modeling through radiative–convective models. *Rev. Geophys. Space Phys.*, **16,** 465–489
Ramanathan, V. and Collins, W.	1991	Thermodynamic regulation of ocean warming by cirrus clouds deduced from observations of the 1987 El Niño. *Nature*, **351,** 27–32
Randall, D. A., Harshvardhan, Dazlich, D. A. and Corsetti, T. G.	1989	Interactions among radiation, convection, and large-scale dynamics in a general circulation model. *J. Atmos. Sci.*, **46,** 1943–1970
Renno, N. O., Emanuel, K. A. and Stone, P. H.	1994	Radiative–convective model with an explicit hydrologic cycle. 1: Formulation and sensitivity to model parameters. *J. Geophys. Res.*, **99** (D7), 14429–14441
Stackhouse, Jr., P. W. and Stephens, G. L.	1991	A theoretical and observational study of the radiative properties of cirrus: Results from FIRE 1986. *J. Atmos. Sci.*, **48,** 2044–2059
Stephens, G. L.	1978	Radiation profiles in extended water clouds. II: Parameterization schemes. *J. Atmos. Sci.*, **35,** 2123–2132
	1984	Review: The parameterization of radiation for numerical weather prediction and climate models. *Mon. Weather Rev.*, **112,** 826–867
Stephens, G. L. and Greenwald, T. J.	1991	The earth's radiation budget and its relation to atmospheric hydrology. I: Observations of the clear sky greenhouse effect. *J. Geophys. Res.*, **96,** 15311–15324

Stephens, G. L., Slingo, A., Webb, M. J., Minnett, P. J., Daum, P. H., Kleinman, L., Wittmeyer, I. and Randall, D. A. 1994 Observations of the earth's radiation budget in relation to atmospheric hydrology. IV: Atmospheric column radiative cooling over the world's oceans. *J. Geophys. Res.*, **99,** 18585–18604

Thuburn, J. and Craig, G. C. 1997 GCM theories for the height of the tropopause. *J. Atmos. Sci.*, **54,** 869–882

Trenberth, K. E. and Guillemot, C. J. 1995 Evaluation of the global atmospheric moisture budget as seen from analyses. *J. Climate*, **8,** 2255–2272

Twomey, S. 1991 Aerosol, clouds and climate. *Atmos. Environ.*, **25A,** 2435–2442

Webster, P. J. 1994 The role of hydrological processes in ocean–atmosphere interactions. *Rev. Geophys.*, **32,** 427–476

Wong, T., Stephens, G. L., Stackhouse, Jr., P. W. and Valero, E. P. J. 1993 The radiative budgets of a tropical mesoscale convective system during the EMEX-STEP-AMEX Experiment. 1. Observations. *J. Geophys. Res.*, **98,** 8683–8693